Signature (supervisor)

MASTER THESIS

Title of the Master Thesis

Polarity compensation on $KTaO_3$ (001) surfaces

Accomplished on the

Institute of Applied Physics
Vienna University of Technology

Submitted by

Flora Josefa Pölzleitner, BSc

Address

Spaunstr. 97, 4020 Linz

Supervisor

Univ.Prof. Dipl.-Ing. Dr.techn. Ulrike Diebold

Co-Supervisor

Univ.Ass. Martin Setvin PhD

Date

Signature (student)

Table of contents

1 Abstract 3

2 Introduction 4

3 Potassium Tantalate $KTaO_3$ 5

3.1 Crystal structure and physical properties of $KTaO_3$ 5

3.2 Motivation for $KTaO_3$ 6

3.3 $KTaO_3$ samples and sample preparation 6

3.3.1 Samples 6

3.3.2 Sample holder 7

3.3.3 Cleaving 7

3.3.4 Sample heating 7

4 Experimental methods 8

4.1 Vacuum technology 8

4.1.1 Types of pumps 8

4.2 Scanning tunneling microscopy (STM) 9

4.2.1 Principle of STM 9

4.2.2 Technical design and instrumentation 10

4.2.3 Imaging artifacts 10

4.3 Non-contact atomic force microscopy (nc-AFM) 11

4.3.1 Principle of nc-AFM 11

4.3.2 Technical design and instrumentation 14

4.3.3 qPlus sensor 14

4.4 X-ray photoelectron spectroscopy (XPS) 14

4.4.1 Principle of XPS 14

4.4.2 Types of lines 15

4.4.3 Technical design and instrumentation of XPS 16

4.5 Low energy ion spectroscopy (LEIS) 17

4.5.1 Principle of LEIS 17

4.5.2 Technical design and instrumentation of LEIS 18

4.6 Low energy electron diffraction 19

4.6.1 Principle of LEED 19

4.6.2 Technical design and instrumentation 20

5 Scanning probe measurements 21

5.1 Characterization of the as-cleaved surface 21

5.2 Annealing experiments 22

5.2.1 Formation of an ordered reconstruction 22
5.2.2 Temperature stability of the labyrinthine structure 24
5.3 Water-induced surface restructuring 27
5.3.1 Dosing 100 L H_2O at room temperature 27
5.3.2 Dosing 300 L of H_2O at room temperature 27
5.4 Water adsorption in the sub-monolayer regime 28
5.4.1 Dosing 1 L of H_2O and annealing at room temperature 28
5.4.2 Dosing 300 L water vapor and annealing at up to 523 K 29
5.5 Annealing after electron bombardment 32
6 XPS measurements 34
6.1 Measurement procedure 34
6.2 Results and discussion of the XPS measurements 34
7 LEIS measurements 37
7.1 Dosing H_2O onto an as-cleaved surface 37
7.1.1 Measurement procedure 37
7.1.2 Results and discussion 37
7.2 Dosing H_2O without intermediate cleaving 38
7.2.1 Measurement procedure 38
7.2.2 Results and discussion 38
8 LEED measurements 39
8.1 Results and discussion of the LEED measurements 39
9 Conclusion 41
10 Abbreviations 42
Table of Figures 43
11 References 45

1 Abstract

This master thesis is focused on the structure of the $KTaO_3$ (001) surface. Along this direction the cleaved surface is polar and several polarity compensation mechanisms are found depending on the applied conditions. In vacuum the as-cleaved surface consists of a mixture of bulk terminated KO and TaO_2 terminated regions. At room temperature defect formation is observed and annealing results in rearrangement of the terraces, while the (1×1) termination is retained. The rearranged surface shows a labyrinthine structure with lines of 4-5 atoms width. This reconstruction is stable for annealing temperatures of up to 723 K. Exposure to water results in a hydroxylated surface and the formation of an overlayer with a (2×1) periodicity. The hydroxylated surface is stable for annealing temperatures of ~373 K and starts to decompose at annealing temperatures of ~473 K. Cleaved $KTaO_3$ single crystals, which are doped by Ba, Yb and Cu, were investigated by atomic force microscopy (AFM), scanning tunneling microscopy (STM), low energy ion spectroscopy (LEIS), X-ray photoelectron spectroscopy (XPS) and low energy electron diffraction (LEED) under ultrahigh vacuum conditions. Experimental details with regard to the sample preparation and the influence of the applied surface science techniques are given. Structural models are proposed based on these experimental results and the stability of these structures is discussed.

2 Introduction

The principal topic of this master thesis is $KTaO_3$ and its behavior under certain conditions. Due to its photoelectrochemical properties $KTaO_3$ is an interesting material for use as anode material in photoelectrochemical cells [1]. It is well known as incipient ferroelectric and the crystal bulk has been investigated under various conditions concerning its dielectric and ferroelectric properties [2-7]. A two dimensional electron gas has been observed on the $KTaO_3$ (111) and (100) surfaces [8,9]. The $KTaO_3$ (001) surface is a suitable substrate for the epitaxial growth of thin films [10,11]. Even superconductivity can be induced at 50 mK by doping with electrostatic carriers [12].

$KTaO_3$ is a cubic perovskite and is built of alternatingly oppositely charged lattice planes [13,14]. This induces a dipole moment perpendicular to the surface and an infinite surface energy. According to Tasker [15] this can be classified as a type 3 surface and is therefore extremely unstable and requires reconstruction or adsorbed species for stabilization. Cleaving the crystal along the (001) lattice plane produces a polar surface that consists of regions of negatively charged KO and positively charged TaO_2 termination. The aim of this master thesis is to characterize the as-cleaved surface and the polarity compensation mechanism in UHV, after annealing and after exposure to H_2O vapor. Thereby the H_2O dosed surface represents a probable configuration that could be expected in ambient conditions and is of particular interest concerning future applications. Also the stability of the respective reconstructions over a certain temperature range is investigated.

In this thesis the structure of the $KTaO_3$ (001) surface was investigated after annealing in UHV and after dosing H_2O. The used crystals were doped by Ba, Yb and Cu, where the Ba doping ensures the electrical conductivity needed for the use of surface science techniques such as STM, LEIS, XPS and LEED. Additionally AFM measurements were carried out to achieve atomically resolved images of the surface. STM was employed to image the structural changes and the stability of the reconstructions. With LEIS the chemical composition of the surface was determined, because He+ ion scattering offers a high surface sensitivity. XPS was used to determine the chemical state of the surface atoms. Also the contribution of the dopant elements to the surface reconstruction was investigated by XPS. Finally LEED patterns were acquired to determine the symmetry of the reconstruction.

In the first part of this thesis the investigation of $KTaO_3$ is motivated and the current state of research is outlined. The crystal structure and the employed samples are described. The next section is dedicated to the experimental methods and the measuring instruments. Some experimental details are explained. Subsequently the measurement results are presented in comparison with numerical calculations and an interpretation of the obtained data with respect to practicality is given.

3 Potassium Tantalate $KTaO_3$

3.1 Crystal structure and physical properties of $KTaO_3$

$KTaO_3$ is a cubic perovskite with a lattice constant of ~3.98 Å [14,16,17]. Along the (001) direction it consists of alternatingly stacked layers of KO and TaO_2 [13,14]. Considering the formal charges of K, Ta and O of +1e, +5e and -2e, respectively, the KO and TaO_2 layers have formal charges of -1e and +1e per unit cell respectively. The stacking of oppositely charged layers makes $KTaO_3$ a 'Tasker type 3' crystal, which demands a surface reconstruction or charged adsorbates to compensate the diverging dipole moment [15]. Below it will be shown that cleaving the crystal in UHV results in a surface consisting of a mixture of KO and TaO_2 terminations. The crystal always cleaves in a way that the topmost layer is a KO plane. Fig. 1 shows sketches of the $KTaO_3$ unit cell, the cleavage plane and the KO and TaO_2 lattice planes.

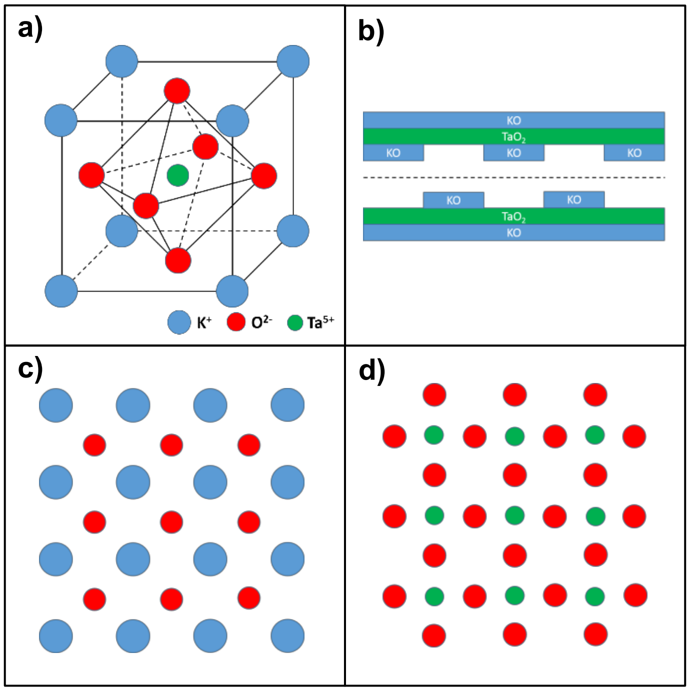

Fig. 1: a) Perovskite structure of $KTaO_3$ b) sketch of cleavage plane c) KO termination d) TaO_2 termination

Pure $KTaO_3$ remains cubic and paraelectric for temperatures down to ~0 K [5,18]. According to references [5,18] $KTaO_3$ is an incipient ferroelectric. This becomes apparent in an increasing dielectric constant for decreasing temperatures and its saturation at a high value (~4000) for temperatures lower than 10 K [2]. Doping can change the intrinsic properties of a crystal including the band structure and optical absorption. For instance Nb-doped $KTaO_3$ crystals show a phase transition from the paraelectric to the ferroelectric state, whereby the transition temperature depends almost linearly with the increasing amount of Nb [19]. Doping $KTaO_3$ with alkaline-earth materials is reasonably practicable and highly increases the electric conductivity [1,20].

3.2 Motivation for $KTaO_3$

Perovskite oxides offer a wide range of applications. Due to their ferroelectric properties perovskites are examined with regard to their potential use in electronic components such as ferroelectric capacitors, ferroelectric field effect transistors and ferroelectric memory [21].

Furthermore perovskites have gained attention because of their photocatalytic properties [22,23]. Ca- or Ba-doped $KTaO_3$ single crystals have been investigated as photoanodic material in photoelectrochemical (PEC) cells, where light is used for the production of electric energy or hydrogen fuel [1]. It was found that they are chemically stable in basic aqueous electrolyte and allow for unassisted photocatalytic water splitting, resulting in the formation of O_2 and H_2 [1]. However the wavelengths suitable for the photocatalytic water splitting with $KTaO_3$ must be <340 nm, whereby the maximum quantum efficiency is reached with 255 nm [1]. As only <2% of the sunlight exhibit appropriate wavelengths, further investigations are necessary to find amounts and sorts of dopants that enable the application of larger wavelengths in photocatalytic water splitting [1]. Composites of reduced graphene oxide and $KTaO_3$ are found to serve for photocatalytic degradation of phenol with visible light [24].

Superconductivity below a critical temperature of ~50 mK can be induced in $KTaO_3$ by electrostatic doping [12].This is a technique that uses high electric fields to accumulate charge carriers in higher densities than it would be possible with the conventional chemical doping method [12].

As demonstrated in reference [9] a two dimensional electron gas (2DEG) can be generated at the (100) surface of $KTaO_3$. Due to polarity of the (100) surface the formation of a 2DEG proceeds faster than in $SrTiO_3$ (100) [9], where similar effects have been reported [25,26]. 2DEGs are of interest with regard to future electronic applications [9].

3.3 $KTaO_3$ samples and sample preparation

3.3.1 Samples

In this thesis $KTaO_3$ single crystals provided by Dr. Lynn A. Boatner from Oak Ridge National Laboratory were examined. The crystals are doped with Ba, Yb and Cu to make them conductive, which is necessary for STM, LEIS, XPS and LEED measurements. Dopant concentrations are in the range of 10^{-4}. Fig. 2 presents pictures of the used $KTaO_3$ single crystals, whereby Fig. 2 a) shows the whole crystals and Fig. 2 b) shows the cleaved surface (arrow 1) that was analyzed by AFM and STM. Arrow 2) points to the AFM tip and the cantilever is marked by arrow 3). Pure $KTaO_3$ single crystals are colorless [17], the dark color of these samples is caused by the doping elements.

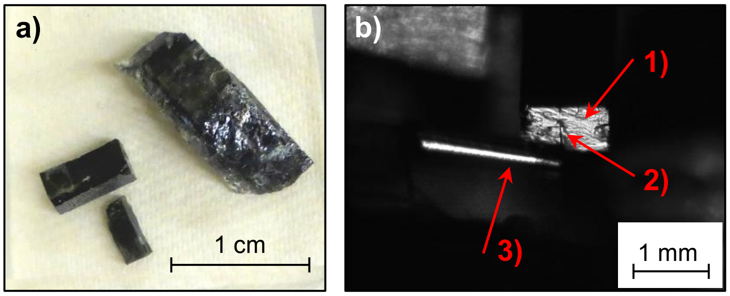

Fig. 2: a) Doped $KTaO_3$ single crystals b) cleaved $KTaO_3$ surface

3.3.2 Sample holder

During the cleaving procedure the sample is subjected to mechanical strain. That is why it is fixed in a special sample holder, where it is clamped between two stainless steel parts that can be adjusted and tightened with stainless steel screws. To prevent the sample from slipping out and to compensate effects of thermal expansion a tiny spring is spot-welded to one of the clamping parts. For the first experiments a stainless steel was used, but with annealing at temperatures higher than about 673 K the steel spring lost its elastic behavior and was deformed permanently. As a result the sample was not properly clamped anymore. For this reason in the STM experiments that require higher temperatures a tantalum spring was employed since its elastic properties are maintained in the desired temperature range.

3.3.3 Cleaving

To provide a completely clean surface a new sample was cleaved before each measurement cycle, which was done on a cleaving stage. The crystal is therefore sustained from one side by a metal bar and cut by a blade from the opposite side of the crystal. To receive a flat cleavage plane with few steps the blade has to cut the crystal exactly perpendicular to the lateral sample surface.

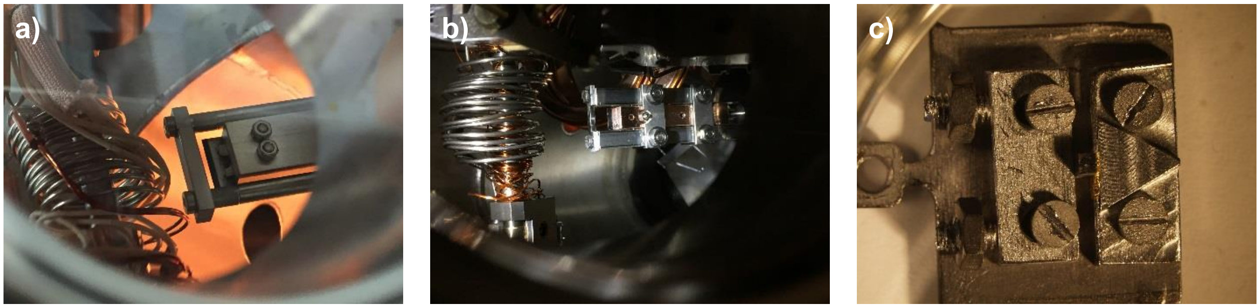

Fig. 3: a) Cleaving stage in the qPlus chamber b) cleaving stage in the LT-STM chamber c) sample holder

3.3.4 Sample heating

Direct heating

In the so called direct heating method a filament, which is situated at the sample manipulator close to the sample plate, is heated and the heat is conveyed to the sample via thermal conduction. This method enables heating to temperatures of up to 873 K, it takes several minutes to reach the final temperature.

Indirect heating

Indirect heating means heating via electron bombardment. Thereby electrons that are emitted from a hot cathode are accelerated onto the sample, where the energy of the electrons is converted into heat. This method allows for fast and local heating to higher temperatures than in the direct heating method. The desired temperature can be achieved within seconds. Indeed when the cooling is performed too fast the sample may fall off the sample plate due to different thermal expansion coefficients of the sample and the fixation.

4 Experimental methods

4.1 Vacuum technology

All the experiments described in the following chapters are carried out in ultrahigh vacuum (UHV), which is due to several reasons. The most obvious reason is to prevent the surface to be investigated from contamination by ambient gas molecules. STM and AFM measurements offer the possibility of achieving atomic resolution, but require a completely clean surface. The same goes for LEIS, which analyses the topmost atomic layer and for LEED and XPS, where the top few atomic layers are examined. A pressure of ~10^{-6} mbar leads to the deposition of one monolayer of impurity atoms within one second [27]. Exposure to ambient atmosphere would immediately cover the whole surface with several layers of impurity atoms and obscure the interesting parts of the surface. Another reason is the inelastic mean free path (IMFP) of particles in a certain atmosphere. Photons, electrons and ions that are used during LEIS, LEED and XPS analysis should be able to traverse the distances between the source, the sample and the analyzer without being deflected or retarded [27]. The usual working pressure is between 10^{-10} and 10^{-12} mbar.

4.1.1 Types of pumps

To reach ultrahigh vacuum conditions, a combination of several different pumps is necessary. An rotary vane pump provides the pre-pressure (up to 10^{-4} mbar [28,29]) for the turbomolecular pump that reduces the pressure in the vacuum chamber down to 10^{-10} mbar [29]. For a further decrease of the pressure (10^{-12} mbar) a combination of an ion getter pump and a titanium sublimation pump is used. In the next section the pumps that were applied during the measurements for this thesis are described.

Rotary vane pump

The rotary vane pump is a mechanical pump that consists of a stator and an eccentrically mounted impeller with two radial arranged vanes. A spring pushes the vanes to the inside wall of the housing, which creates two separate rotating chambers. On the low pressure side gas flows into one chamber, is expanded and compressed again. When the pressure exceeds the atmospheric pressure, an outlet valve is opened and the gas molecules are transported outside the chamber [28,29].

Turbomolecular pump

A turbomolecular pump consists of alternatingly arranged stator and rotor blades, whereby the rotor is driven at a frequency of ~1 kHz. The gas particles are moved away from the low pressure side by a directed momentum transfer from the blades. In combination with a backing pump a vacuum pressure of ~10^{-10} mbar can be achieved [29].

Ion getter pump

Ion getter pumps consist of hollow cylindrical anodes, where a potential of ~5 kV is applied [29]. On each end of the anode a grounded cathode is placed that is composed of a chemically reactive metal [29]. In most applications titanium is used as cathode material. A magnetic field in the direction of the cylinder axis causes electrons that are attracted by the anode to move in circles around the anode [29]. On their way the electrons ionize gas molecules. Thereby more electrons are produced resulting in an electron cascade [29]. The ions are accelerated towards the cathodes, where they penetrate the surface up to one micrometer [29]. Here they are neutralized and captured beneath the surface [29], so no mechanical pumping is necessary to remove the gas particles. Ions, that are neutralized before they reach the cathode or are reflected from the cathode as neutral particles,

$$A = \frac{4\pi}{h} \cdot (2m)^{1/2} = 1.025\ \text{Å}^{-1} eV^{-1/2} \qquad \text{Eq. 2}$$

φ is the height of the tunnel barrier (work function), z is the width of the tunnel barrier (tip-sample distance), h is the Planck constant and m is the mass of a free electron. This exponential dependence between the tunneling current and the tip-sample distance is the reason for the high resolution that can be reached with STM. From Eq. 1 it is apparent that in measurements with constant tunneling current the product $\varphi^{1/2}z$ has to be constant, which implies that the measured signal only reflects the real sample topography if the work function is constant [30-32]. In general the tip moves along lines of constant local density of states (LDOS) at the Fermi energy E_F [32]. The structure in an STM image can therefore be caused by a topographic feature, a change in the work function or by local variations of the density of states.

4.2.2 Technical design and instrumentation

Positioning of tip and sample

For the positioning of the sample piezoelectric driven inertial sliders are used [32-35]. The operating principle is based on the stick slip effect. Thereby a shear piezo is placed between two electrodes, between which a sawtooth voltage is applied [34]. The increasing voltage causes the piezo to extend and move one of the electrodes, while the second electrode stays at its position [34]. When the force onto the second electrode exceeds the frictional force, the second electrode slips to the level of the first electrode and the whole sequence is repeated [32-35]. Using three piezo elements enables three dimensional movement of the sample.

The scanning motion of the tip is also realized via piezo drives, whereby different geometries are possible like piezoelectric bars [31], tubes [36] and bimorphs [32].

Vibration isolation

The most important framework condition for high resolution measurements in the Å range is a vibration isolation. Typical amplitudes of floor vibrations are in the range of micrometers and therefore would not allow for vertical resolutions in the range of picometers [32]. In this thesis vibration isolation was realized via pneumatic feet or a damping system based on a system of bungee cords.

Tip and tip preparation

The tips applied in STM were fabricated by electrochemical etching of a tungsten wire and KOH was used as the etching liquid. To achieve atomic resolution it is important to use a preferably monoatomic tip. Additional atoms with the same tip-sample distance cause so called multiple-tip-imaging artifacts. Due to the exponential dependence of the tunneling current with respect to the distance, atoms that are situated more than ~3 Å further away from the sample than the topmost atom, almost do not contribute to the tunneling current anymore [32]. For the investigation of rough surface structures it is important to use tips with small cone angles. Otherwise the images do not show the real corrugation, as the tip cannot trace the complete surface structure without mechanical contact [32].

4.2.3 Imaging artifacts

Tip artifacts

STM images represent a convolution of the electronic structure and the shape of the sample and the tip [32,37]. This entails several imaging possible imaging artifacts. Atoms that fall off or get stuck to the tip change the electronic structure of the tip and thereby the measuring signal [32]. This effect can also be useful to detect different elements or to increase the resolution [32]. Another artifact is the so called tip imaging [37,38]. If the surface feature is sharper than the tip the STM image shows the shape of the tip and not the sample surface [37,38]. A similar effect occurs for undercut features, where the side of the tip is imaged instead of the real surface profile resulting in the broadening of the imaged features [37]. For a tip with more than one atom at the position closest to the sample the surface features are imaged several times, which is called multiple tip artifact. By applying a bias pulse the redundant multiple tips can be removed via field emission [38] and in the ideal case a monoatomic tip remains.

Scanning artifacts

In the ideal case the dimensions of a piezoelectric element scale linearly with the applied electric field. This can be expressed via the strain of the piezoelectric element [38]:

$$s = \frac{\Delta l}{l} = Ed \qquad \text{Eq. 3}$$

Thereby s is the mechanical strain, l is the original length, Δl is the change in length, E is the electric field and d is the strain coefficient. In reality several factors exist that cause a deviation from this ideal behavior. There is an intrinsic nonlinearity that is reflected in irregularly spaced measurement spots leading to a curved depiction of straight features [37,38]. Hysteresis effects cause a different scanner extension for increasing and decreasing voltages depending on size and rate of the voltage change and the scan angle [37,38]. This effect becomes apparent in images of the same sample region that look different depending on the scan direction [38]. Hysteresis can often be compensated by a software [37]. Piezo creep occurs after sudden voltage changes, for example after moving the scanner to a different position on the sample or changes of the scan speed, and manifests as differences in the length scale [37,38]. As it is a time dependent effect, it is balanced after a few scan lines [37]. Another effect called cross coupling refers to the coupling of the motion in z-direction to the motion in x- and y-direction and results in a bowing in the image of an even surface [37,38]. All these nonlinearities affect the imaging in x- and y-direction as well as in the z-direction, where they lead to inaccuracies in height measurements. The imaging errors in the x-y-plane can generally be compensated by software, while the inaccuracies in the height measurements can only partly be canceled out by software and calibration with height standards [37,38].

Thermal drift

Another reason for image distortions is thermal drift. It appears due to small temperature variations that cause a thermal expansion, which, in turn changes the adjustment of the tip and therefore the image [39]. To minimize the thermal drift, the scanning unit as well as the sample are placed in a cryostat [39] and after the sample has been inserted into the scan head it is left to cool down completely before measurements is being performed.

4.3 Non-contact atomic force microscopy (nc-AFM)

4.3.1 Principle of nc-AFM

AFM is a surface science technique that uses the deflection of a cantilever caused by the forces between the tip and the sample and allows for atomically resolved images. The experiments in this thesis were performed in the frequency modulation mode. Thereby the cantilever oscillates at a constant amplitude, while it is scanned across the surface to be investigated. The oscillation frequency varies depending on the tip-sample force and this so-called frequency shift is proportional to the gradient of the force acting on the tip. Images are constructed by recording the frequency shift as a function of the position on the sample.

The free oscillation frequency f_0 is described by [40]

$$f_0 = \frac{1}{2\pi}\sqrt{\frac{k}{m^*}} \qquad \text{Eq. 4}$$

where k is the cantilever stiffness and $m^*$the effective mass. The oscillation frequency f in presence of the tip-sample potential reads [40]

$$f = \frac{1}{2\pi}\sqrt{\frac{k + \langle k_{ts} \rangle}{m^*}} \qquad \text{Eq. 5}$$

where k_{ts} is the stiffness attributed to the tip-sample potential V_{ts} by $k_{ts} = \partial^2 V_{ts}/\partial z^2$ and $\langle k_{ts} \rangle$ is the average stiffness according to [41]

$$\langle k_{ts} \rangle = \int_{-a}^{a} k_{ts}(x, y, z + z') \frac{\sqrt{a^2 - z'^2}}{\pi a^2/2} dz' \qquad \text{Eq. 6}$$

when the cantilever moves from $-a$ to a. By assuming that $\langle k_{ts} \rangle$ is small compared to k the square root in Eq. 4 and Eq. 5 can be approximated by a Taylor series leading to an expression for the frequency shift [40].

$$\Delta f = f - f_0 \cong f_0 \frac{\langle k_{ts} \rangle}{2k} \qquad \text{Eq. 7}$$

From Eq. 7 it is clear that the frequency shift depends on both the stiffness of the cantilever and the tip-sample potential, which implies the tip-sample force.

The tip-sample potential can be described by a Lennard-Jones potential [42-44], which is outlined in Fig. 5. In Eq. 8 the mathematical description of the potential is given [42-45]:

$$V_{ts}(z) = 4\varepsilon\left(\left(\frac{z_m}{z}\right)^{12} - \left(\frac{z_m}{z}\right)^{6}\right) \qquad \text{Eq. 8}$$

Thereby z is the tip-sample distance, ε is the depth of the potential well and z_m is the distance, where $V = 0$. The tip-sample force F_{ts} is the first derivative of V_{ts} with respect to the tip-sample distance, $F_{ts} = \partial V_{ts}/\partial z$, and at z_{eq} the tip-sample force is zero. For distances $z > z_{eq}$ the tip-sample force is attractive, which is caused by van der Waals interactions, electrostatic forces and short range chemical forces [42,43]. When the tip is brought close to the sample $(z < z_{eq})$ the electronic orbitals overlap, creating a strongly repulsive region due to the Pauli exclusion [43].

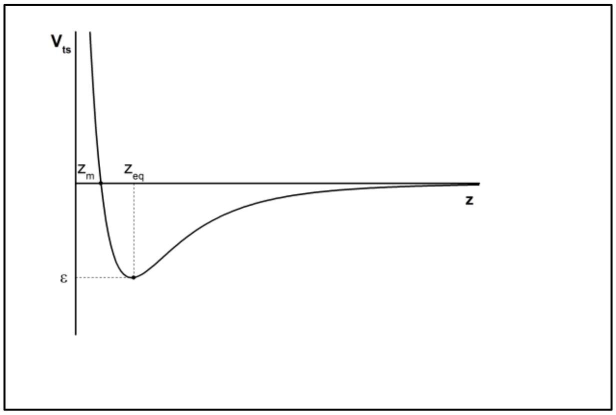

Fig. 5: Lennard-Jones potential, where r is the tip-sample distance and ε is the depth of the potential well. At r_m the potential is zero and at r_{eq} the total force is zero.

AFM measurements usually take place in the attractive region [40,44]. The three main contributions to the attractive force (van der Waals interactions, electrostatic and chemical forces) have different interaction ranges, so depending on the tip-sample distance different forces are pronounced. Atomic resolution is achieved by analyzing the short range forces [43]. Van der Waals forces are long range forces and moreover involve many atoms in the tip as well as in the sample, which makes them unsuitable for atomic resolution [43]. In general the interaction ranges of electrostatic forces are even longer than the ranges of the van der Waals forces. Indeed for ionic crystals they contribute to the short range forces as the electrostatic forces of the individual anions and cations cancel out each other at longer distances but can be distinguished at short distances [43]. Chemical forces (e.g. covalent bonding interaction) are short range forces and are therefore used to achieve atomic resolution in covalent crystals and semiconductors [43].

Two different imaging modes were applied: the constant frequency shift mode and the constant height mode. For measurements in constant frequency shift mode a feedback loop is employed that levels the distance between the tip and the sample so that the frequency shift is constant, while the tip-sample distance is recorded. This mode is applied on unknown surfaces to obtain a first rough image of the surface. On flat surfaces the constant height mode is applicable. Thereby the tip is kept at a constant height, while the frequency shift is recorded. With constant height mode the acquisition of highly-resolved images is possible, because the tip-sample distance can be arbitrarily small. On the downside the constant height mode harbors the risk of a tip crash in case there is an unexpectedly high surface feature.

In AFM the imaging signal is the force between the tip and the sample, which implies several differences and improvements compared to STM [40,42]:

- For AFM no electric conductivity is required, which makes it suitable for the examination of both conducting and non-conducting samples.
- As the force is non-monotonic with respect to the tip-sample distance, a sophisticated feedback system is necessary.
- In addition to the topmost atom all the atoms at the tip apex contribute to the imaging signal. This leads to a higher background signal and a strong dependence on the sorts of atoms that are stuck to the tip apex.

4.3.2 Technical design and instrumentation

As the frequency shift is strongly affected by the geometry and the composition of the tip [46] it is essential to use well defined, monoatomic tips. For reasons of stability and resolution several conditions concerning cantilever stiffness k, the oscillation amplitude A and the quality factor Q have to be met [40,42,43]. The restoring force of the cantilever is given by kA and its value has to be sufficiently large compared to the tip-sample force to permit stable oscillations [40,42,43]. This can be achieved by using a stiff cantilever with small amplitudes, or by operating a soft cantilever at appropriately large amplitudes [40,42,43]. The use of stiff cantilevers with small amplitudes has proven to yield atomic resolution in several cases (see [40,42,47,48]), because the use of small amplitudes offers higher sensitivity to short range forces and the high stiffness improves the signal-to-noise ratio [42]. A typical value for the spring constant of a stiff cantilever is 10^3 Nm^{-1} and a typical amplitude is ~1Å [42,47,48]. The Q factor describes the damping of the system, whereby a high Q factor stands for a light damping. Measurements in frequency modulation mode that are carried out in UHV reveal extremely high Q factors of ~10^5 compared to Q factors of ~100 in slope detection measurements, where the cantilever is oscillating at a fixed frequency close to resonance [49].

Another aspect that must be treated is the energy balance of the cantilever. Due to internal friction and hysteresis effects in the tip-sample forces the cantilever loses energy. To maintain the constant amplitude condition the energy difference is settled by the amplitude controller [40,42], which is only possible for hysteresis energy losses that are small compared to the intrinsic losses [40,42]. The measurement signal is subject to noise caused by thermal vibrations of the cantilever and electronic noise [49]. Both types of noise show a dependence of 1/A on the amplitude [42]. In combination with the signal as function of the amplitude a maximum of the signal-to-noise ratio is obtained, if the amplitude is set to a value close to the range of interaction of the present forces [40]. The positioning of the sample and the sensor is implemented in the same way as in STM and therefore also the same imaging artifacts caused by the scanner take place as discussed in sections 4.2.2 and 4.2.3.

4.3.3 qPlus sensor

A qPlus sensor allows for simultaneous acquisition of STM and AFM images. For stability reasons cantilevers with high stiffness (~1 kNm^{-1}) and frequency stability [40] are needed. Quartz tuning forks fulfill these requirements in addition to a high temperature stability of the frequency and the possibility for electrical deflection measurements [40]. The tuning forks consist of two prongs of which one is fixed and on the other one the tip is mounted. This provides a constant Q-factor during the whole scanning procedure [40] and prevents mixed modes of the oscillations of both prongs. Two electrodes on the tuning fork provide the connection to the tip bias voltage and the measurement of the cantilever deflection [40]. The sensor can be operated using a feedback loop in STM constant current mode or in AFM mode with constant frequency shift. Thereby the tip height is adjusted according to the measurement variable that is to be kept constant, but both, the tunneling current and the frequency shift, are detected. Additionally the measurements can be carried out in constant height mode, where again, both the tunneling current and the frequency shift are detected.

4.4 X-ray photoelectron spectroscopy (XPS)

4.4.1 Principle of XPS

In XPS the surface is probed with X-ray photons that cause the emission of core level electrons via the photoelectric effect. The kinetic energy of these photoelectrons is detected, since it carries information about the chemical composition, the oxidation state and the electronic structure of the investigated surface [27,50,51]. Thereby the kinetic energy of the photoelectrons that is measured by the spectrometer (with reference to the spectrometer work function ϕ_{spec}) is given by

$$E_k = E_{h\nu} - \phi_{spec} - E_b \qquad \text{Eq. 9}$$

with the kinetic energy E_k, the energy of the incident photons $E_{h\nu}$ and the binding energy of the photoelectrons E_b. It is noteworthy that the measured signal does not depend on the work function of the sample [27,51]. In XPS the electron count rate is plotted as a function of the kinetic or binding energy. Each element exhibits a characteristic set of core level peaks, which allows for the analysis of the chemical composition [27,50,51]. For each chemical compound the positions of the core level peaks are slightly shifted (chemical shift) compared to their elemental peaks. This provides information on the chemical state [27,50,51]. The surface sensitivity of XPS is attributed to the short mean free path (a few Å) of the photoelectrons in solids [27,50,51]. Only hydrogen and helium cannot be detected by XPS as they exhibit small cross sections for photoionization [52].

4.4.2 Types of lines

An XPS spectrum contains several types of lines that correspond to different physical effects.

Core level peaks

As already mentioned, the core level peaks are caused by the electrons emitted due to the photoelectric effect. Each element shows a characteristic set of core level peaks with specific relative intensities [51]. By measuring their peak height or peak area the percentage of the respective elements can be estimated, whereby the analysis of the peak area yields more precise results [51]. As each element is detected with a specific probability, the peak areas must be divided by so called atomic sensitivity factors [51]. By precisely defining the peak positions conclusions about the chemical environment can be drawn [27,50,51].

Auger peaks

After the emission of the photoelectron the excited ion relaxes by filling the inner orbital vacancy with an electron from an outer orbital. The redundant energy is transferred to another electron (the Auger electron) that is emitted too, leaving a twofold charged ion [51]. As the energy difference between the orbitals is independent of the original excitation energy, Auger peaks appear at different binding energies when the measurements are performed with different anodes. When the kinetic energy is plotted, the Auger peaks remain at the same positions [51]. Like the core level peaks the Auger peaks appear at characteristic positions, but have rather indefinite peak shapes. This is why the information provided by Auger peaks is less obvious and the analysis of the core level peaks is preferred in XPS [27].

X-ray satellite peaks

If nonmonochromatic X-rays are applied in the XPS analysis, the photoexcitation is caused by several different energies additional to the most intense center excitation energy. This leads to additional peaks that are situated at a certain distance from the primary peak and have a specific intensity compared to the core level peaks [27,51]. They can therefore be easily identified.

Shake up satellite peaks

Shake up lines are produced when when a valence electron is excited during the photoemission, which reduces the kinetic energy of the photoelectron leading to an additional peak at higher binding energies than the respective core level peak [27,51].

Multiplet splitting

Multiplet splitting takes place for photoemission in atoms with unpaired valence electrons. As there are several possibilities for the spin coupling of the remaining core electron with an outer electron, several final states of the ion occur. This is apparent in the splitting of the photoelectron line [51].

Ghost lines

Ghost lines appear if the X-radiation originates not only from the chosen anode but for example from the housing material of the X-ray gun, another anode (if more than one anode is present) or from the sample itself [51]. Thereby the latter case rarely appears because the probability for X-ray emission of the sample is small compared to the probability of Auger emission [51].

Energy loss lines

The photoelectron can lose energy to group oscillations of the bulk or the surface. The energy loss is characteristic for each material and emerges 20-25 eV above the binding energy of the respective core level peak [51].

Background signal

The background signal in XPS spectra is determined by inelastic energy losses of the photoelectrons on their path through the sample and by the amount of bremsstrahlung in the X-radiation. Energy losses of the photoelectrons result in a higher background on the higher binding energy side of a core level peak [27]. Bremsstrahlung causes a generally increased background signal for higher binding energies [27,51].

4.4.3 Technical design and instrumentation of XPS

X-ray source

To yield adequate measurement results X-ray sources used in XPS need to fulfill several requirements concerning the photon energy, energy resolution and applicability [27]. The photon energy must be high enough to excite photoemission in the whole range of elements, whereby the full width at half maximum (fwhm) must be small enough to allow for the resolution of chemical shifts [27]. These conditions are met by the Al Kα radiation (hv = 1486.7 eV, fwhm = 0.85 eV) and the Mg Kα radiation (hv = 1253.6 eV, fwhm = 0.7 eV) [27]. In many XPS systems a twin anode is applied that enables the user to choose between the Al and the Mg radiation [27,53]. This is convenient in the case that Auger lines obscure core level peaks that are essential for the analysis [27]. For elements with core level peaks at high binding energies the Al anode is preferred, while the Mg anode provides a better resolution for core level peaks at lower binding energies. The technical realization of a twin anode is shown in the sketch in Fig. 6. Thereby electrons are emitted from a filament and accelerated onto the anode resulting in the emission of characteristic X-radiation and bremsstrahlung. To protect the sample from influences of the fields and contaminations by the filament the X-ray source is placed in a housing with an Al window. The Al window is a few µm thick [27] and allows the characteristic X-radiation to pass, while electrons and a part of the the bremsstrahlung is reduced [27]. As the emission of such intense X-rays requires high electric power the X-ray source needs a sufficient water cooling [27].

Hemispherical analyzer

The energy analysis of the photoelectrons is implemented via a hemispherical analyzer. This kind of analyzer is built by two concentric hemispheres on which certain voltages are applied [27]. Electrons that enter the analyzer are deflected according to their kinetic energy. Only electrons with the so called pass energy can traverse the analyzer and reach the detector [27]. In practical measurements the pass energy is set to a constant value to achieve a constant energy resolution [27,51]. A system of electronic lenses that is placed between the sample and the analyzer entrance retards or accelerates the electrons so they finally have the pass energy [27,51]. By scanning the adjustment of the lens system the intensity depending on the kinetic energy can be plotted. The choice of the pass energy determines the energy resolution: a low pass energy implies high resolution [27].

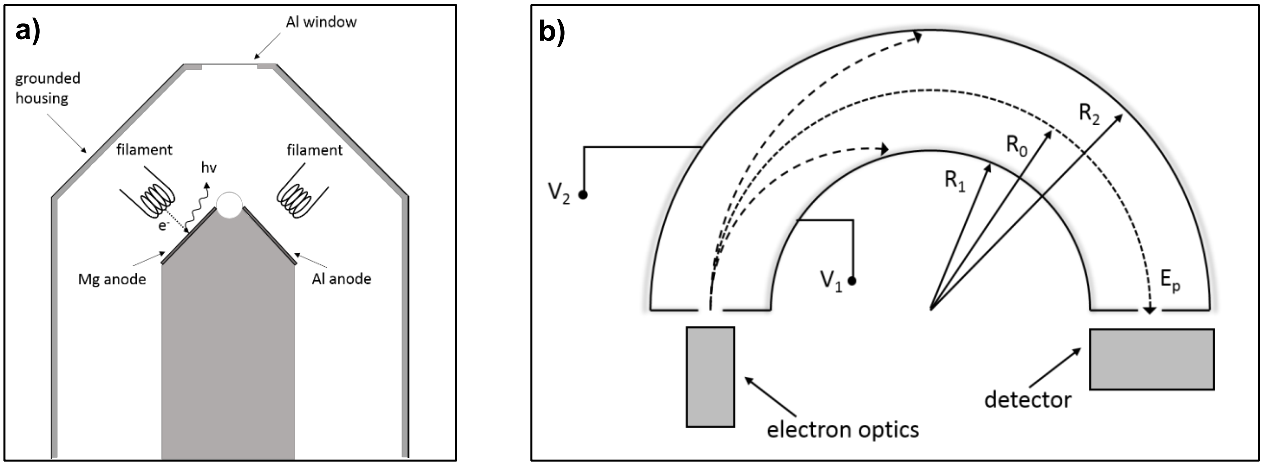

Fig. 6: a) Schematic of an X-ray source with twin anodes based on [53] b) schematic of hemispherical analyzer based on [27]

Detector

The electrons that pass the analyzer are detected in channel electron multiplier. This is built of a curved ceramic channel, which provides a high emission of secondary electrons upon the impact of photons, electrons and ions [54,55]. The secondary electrons produce further electrons finally leading to a multiplication of up to 10^8 [56], which produces a measurable current. Between the entrance and the end of the multiplier channel a high voltage of a few kV is applied to direct the electrons towards the output [56].

4.5 Low energy ion spectroscopy (LEIS)

4.5.1 Principle of LEIS

LEIS is a surface science technique for analyzing the chemical composition of the topmost atomic layer of a sample. This is implemented by directing noble gas ions onto the sample and analyzing the energy of the backscattered ions that depends on the mass of the atoms the ions are scattered on: the smaller the mass of the surface atom, the higher the kinetic energy of the detected ion. The energy of the ions is about 1-3 keV [57], which is the reason for the high surface sensitivity of LEIS. On one hand the energy is low enough to avoid a strong penetration of the sample, on the other hand it allows only the ions that are scattered at the outermost surface layer to reach the detector before being neutralized [57,58]. The energy E_S of the scattered ion can be described by the following equation:

$$E_s = \kappa \cdot E_p = \left(\frac{\cos(\theta) + \sqrt{\left(\frac{M_s}{M_p}\right)^2 - sin^2(\theta)}}{1 + \frac{M_s}{M_p}} \right)^2 \cdot E_p \qquad \text{Eq. 10}$$

Thereby E_p is the energy of the impinging ion, M_s is the mass of the surface atom, M_p is the mass of the impinging ion, κ is called the kinematic factor and θ is the scattering angle defined by Fig. 7 [57]. To ensure that the ions are scattered back $\frac{\mathrm{M_s}}{\mathrm{M_p}} \geq 1$ must be fulfilled. Eq. 10 also tells that the higher M_s is in comparison to M_p the closer the energy of the scattered ion approaches the energy of the incoming ion [58,59]. For this reason hydrogen cannot be detected directly [57].

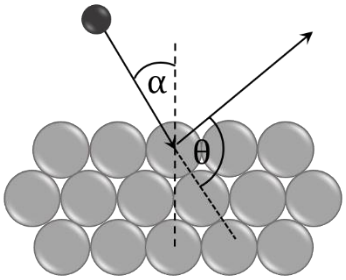

Fig. 7: Schematic for the definition of the scattering angle θ and the incident angle α.

LEIS provides energy spectra that plot the intensity as a function of the kinetic energy of the backscattered ions. The surface information is contained in the so called elastic binary collision peak, which is produced by ions that have undergone a single scattering process [57]. The width of the binary collision peaks is determined by the energy spread and the angular spread of the incident ions [57]. For this reason a low energy and angular spread of the incoming ions is required to receive an acceptable resolution [57]. Another factor that influences the peak width is neutralization. For a high neutralization probability it is unlikely that an ion is scattered more than once without being neutralized, so the main contribution to the backscattered intensity comes from single scattering events [57]. If the neutralization probability is low, ions that were scattered several times are detected leading to a tail of the binary collision peak towards lower energies [57]. Ions that reach deeper layers of the sample before they are scattered back or ions that are neutralized and reionized have lost some of their energy at the collisions. Again this becomes apparent in a low energy tail [57]. The intensity of the binary collision peak is defined by the acquisition time, the elemental sensitivity factor, the analyzer transmission and the detector efficiency [57].

4.5.2 Technical design and instrumentation of LEIS

Electron impact ion source

In an electron impact ion source noble gas atoms are ionized by electrons that are produced by a filament and accelerated by an applied voltage. Extraction of the ions from the ionization chamber and focusing is accomplished by electrostatic lenses. The ion beam can be scanned in a grid, which is used to find the optimum measurement position on the sample. Two different focusing methods are applied:

The classical focusing method implies the measurement of the sample current as a function of the scanning position of the ion beam. On an oscilloscope the current intensity is made visible, which allows for the determination of the position of the sample plate. As the sample itself is not discernible, the ion beam is focused on the estimated sample position.

As the lateral surface of the investigated crystals is considerably larger than the cleaved surface, a precise focusing is necessary to receive the information only from the cleaved surface. This is achieved by using STM scanning electronics and an STM software instead of the usual ion gun electronics and the oscilloscope. The STM electronics enable both a more precise positioning and a higher resolution of the measured current. In this way also the sample is rendered visible and the differentiation between the lateral and the cleaved surface is possible. Hence the ion beam is focused exactly onto the cleaved surface.

Analyzer and detector

For the energy measurement and the detection of the backscattered ions the same hemispherical analyzer and channel multiplier are applied as in XPS (described in 4.4.3). Via the control software the system (retarding lenses and analyzer) can be adjusted to positive particles. Again the ions are retarded in front of the analyzer to reach the pass energy and are detected after passing the analyzer [57,59]. Due to the geometry of the hemispherical analyzer only a small amount of the backscattered ions reaches the detector, resulting in a faint measurement signal [57,59]. For this reason high pass energies are used in LEIS.

4.6 Low energy electron diffraction

4.6.1 Principle of LEED

LEED involves an electron beam that is directed onto a single crystal and the detection of the diffracted electrons. The applied electron energies are between 10 and 500 eV [60], which corresponds to wavelengths of 1-0.1 Å [60]. Thereby the magnitude of the wavelengths is in the range of typical atomic distances and thus allows for resolution of structures on the atomic scale [60]. As electrons of these energies have an inelastic mean free path of a few Å [61], the backscattered electrons carry information of the first few atomic layers and are responsible for the high surface sensitivity of LEED [60].

When the electrons directed onto the sample surface, they can be scattered inelastically and elastically. On the fluorescent screen a pattern of bright spots is visible, determining the spots of constructive interference of the elastically scattered electrons. Elastic scattering or diffraction of the electron is described by Bragg´s equation:

$$2d\, sin(\alpha) = n\lambda \qquad \text{Eq. 11}$$

Thereby d is the lattice constant, α is the angle between the backscattered electrons and the lattice plane, λ is the wavelength of the incident electrons and n is an integer. According to Eq. 11 the diffraction pattern changes with changes of the wavelength of the incoming electrons. Thereby both the positions and the intensity of the diffraction spots changes, which gives several types of information. Kinematic LEED is the analysis of the diffraction pattern for a fixed wavelength. Information about periodicities and size and shape of the surface unit cell are gained [62] but no quantitative statement can be made. Adsorbates result in additional diffraction spots or a change of the spot intensities [60]. The so called dynamic LEED involves the measurement of the intensities of several diffraction spots for varying wavelengths or incident angles of the impinging electrons [60]. This method enables the determination of the arrangement of atoms within the unit cell, indeed it requires the comparison with theoretical calculations [60,62]. Another technique is the spot profile analysis LEED (SPA-LEED), which allows for the identification of surface imperfections [62]. In this theses only kinematic LEED is used as supplementary analysis method for the proof of superstructures.

4.6.2 Technical design and instrumentation

An electron gun that is based on a filament produces a beam of electrons with a certain energy that is focused onto the sample surface. The impinging electrons can either be scattered inelastically (secondary electrons) or elastically (diffracted electrons), whereby the amount of elastically scattered electron is only 2-5 % [60]. As the information about the crystal lattice is provided by the elastically scattered electrons, the inelastically scattered electrons must be selected. This is implemented by a retarding grid, where a slightly negative voltage is applied that allows only the elastically scattered electrons to pass [60]. Between the third grid and the fluorescence screen a highly positive voltage is applied to accelerate the electrons and direct them onto the screen, where they are detected as light emission [60]. As low energy electrons are sensitive to the earth magnetic field their trajectories would be changed without a compensation method [63]. One possible technique that was applied in this thesis is the use of a pair of Helmholtz coils to provide a homogeneous magnetic field. In Fig. 8 a) a schematic of a LEED apparatus is presented and Fig. 8 b) shows a picture of the LEED instrument used in this thesis. The fluorescent screen can be viewed through a vacuum window (1) and the coil for the compensation of the earth magnetic field is labeled (2).

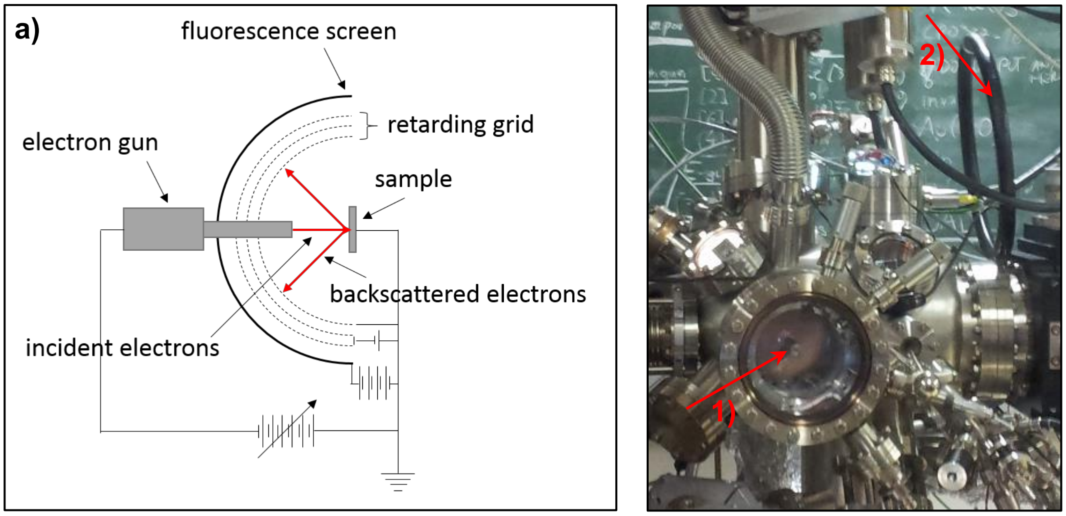

Fig. 8: a) Schematic of a LEED apparatus based on [60] b) picture of LEED instrument (1) and coil (2)

5 Scanning probe measurements

5.1 Characterization of the as-cleaved surface

Prior to the experiments the samples were degassed at ~873 K via direct heating. To prepare a clean surface the crystal was cleaved in a cleaving stage, whereby the quality of the cleavage plane depends on various factors like the temperature, the cleaving angle and the homogeneity of the sample. The surface therefore looks slightly different for each cleaving procedure. This is recognizable by the two examples shown in Fig. 9 a) and Fig. 9 b).

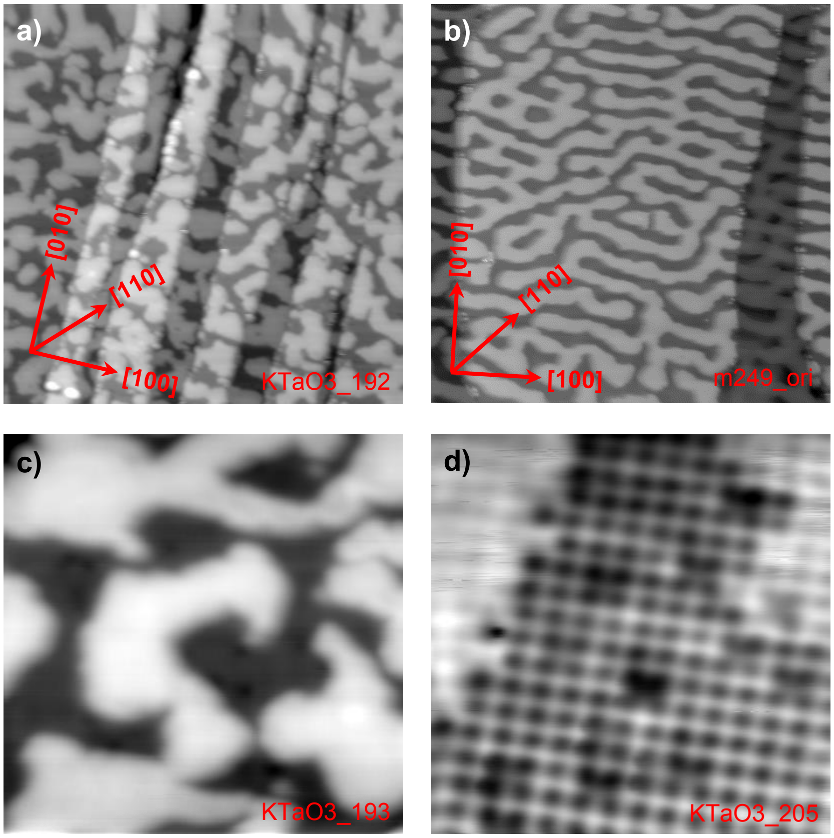

Fig. 9: a) Cleaved at room temperature, STM, 100×100 nm², 3.0 V, 0.01 nA b) cleaved at 350 K, STM, 100×100 nm², 3.5 V, 0.1 nA c) cleaved at room temperature, STM, 25×25 nm², 3.0 V, 0.01 nA d) cleaved at room temperature, AFM, 5×5 nm², 0.45 V

For the images in Fig. 9 a), c) and d) the sample was cleaved at room temperature and scanned at 78 K. In Fig. 9 a) one can see that the crystal cleaves in elongated stripes along the [010] direction and the terraces consist of structures without a specific symmetry. To point out that different cleaving conditions yield different surface textures Fig. 9 b) shows the surface after cleaving at 350 K. Compared to the previous images a) the surface now looks smoother and reveals less steps. The KO regions exhibit an average width of ~6 nm. Each terrace contains a brighter and a darker layer of which the brighter ones are KO terminations and the darker ones are TaO_2 terminations. The differentiation between the two terminations was made by reference to the electronic structure that is determined by scanning tunneling spectroscopy. LEIS spectra that are presented in 7.2.2 point out that the KO termination is always on top. In STM no atomic resolution can be achieved, hence AFM is necessary to obtain a higher resolution. Fig. 9 d) shows a constant height AFM image of the as-cleaved surface. There are regions of atomic resolution that correspond to the bright regions in the STM image. With regard to the crystal structure of $KTaO_3$ [13] the dark pattern indicates the KO layer. Since the contrast in AFM depends on whether the tip is terminated by an anion or cation [64] it cannot be determined whether the dark spots correspond to K or O. The diffuse areas that appear bright in the AFM image should belong to the TaO_2 layer. Unfortunately these regions cannot be atomically resolved. The pattern that is visible on the bright regions is the effect of a double tip.

5.2 Annealing experiments

5.2.1 Formation of an ordered reconstruction

The formation of an ordered reconstruction upon different annealing temperatures was measured in a q-Plus instrument by STM and AFM at the temperature of both liquid nitrogen and liquid helium.

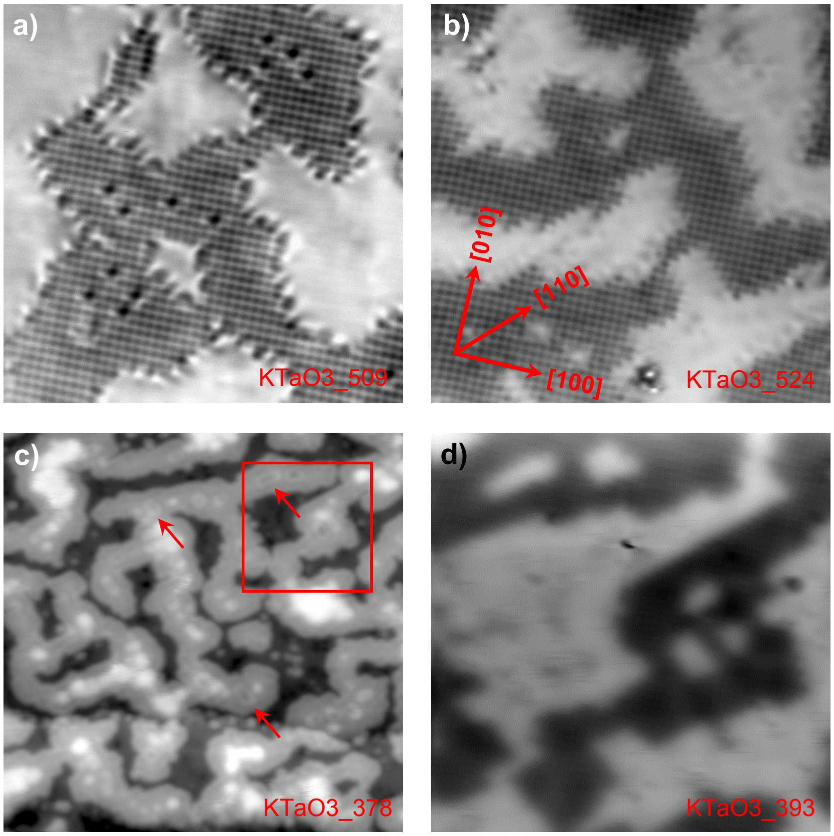

Fig. 10: a) As-cleaved surface, AFM, 17×17 nm², -0.2 V b) surface after annealing at 371 K, AFM, 18×18 nm², -0.5 V c) surface after annealing at 387 K, STM, 60×60 nm², 3.2 V, 0.002 nA d) surface after annealing at 387 K, AFM, 18×18 nm², 0.1 V

Fig. 10 a) shows an AFM image of the sample after cleaving at 325 K in UHV, where some black spots are visible on the topmost KO layer. A first annealing step was done at 371 K for ten minutes (see Fig. 10 b)) and it is apparent that the black features have disappeared. They could be crystal impurities or dopants that move to the bulk with annealing. Also the beginning of the formation of straight step edges can be observed. For the images in Fig. 10 c) and d) the sample was cleaved at 231 K and annealed at 387 K for ten minutes in UHV. Regarding Fig. 10 c) one can see holes developing in the KO layers, the arrows point to some of these holes. The constant height AFM image (Fig. 10 d)) shows the area marked in Fig. 10 d) in more detail.

To investigate the further development of the structure with the temperature the sample was annealed at 426 K for 15 minutes (see Fig. 11).

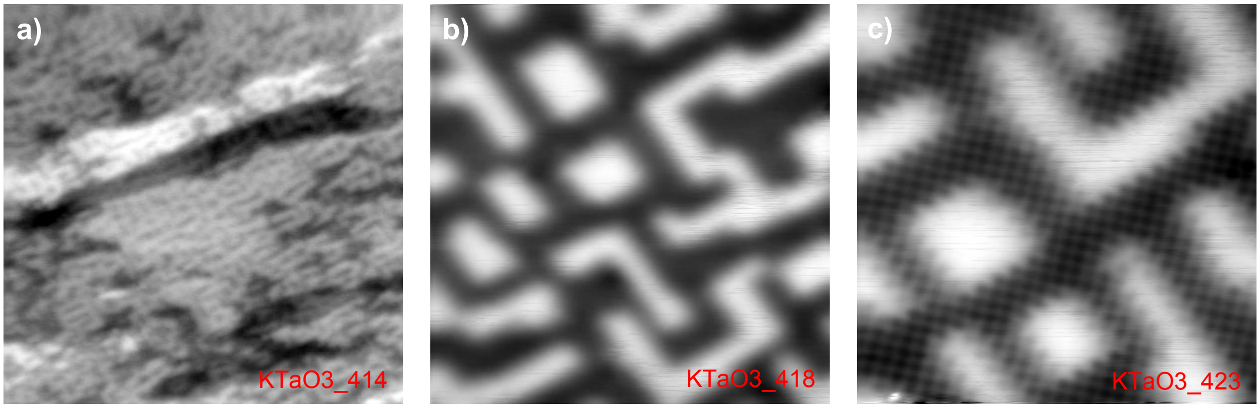

Fig. 11: KTaO$_3$ surface after annealing at 426 K a) AFM, 100×100 nm², 0.001 V, -1.8 Hz b) AFM, 16×16 nm², 0.001 V c) AFM, 10×10 nm², 0.001 V

The large scale AFM image (Fig. 11 a)) shows that the surface has completely rearranged and a labyrinthine structure has appeared. Fig. 11 b) and c) show more detailed constant height AFM images. They reveal that the edges between the upper KO layer and the lower TaO$_2$ layer run along the [110] and the [-110] direction.

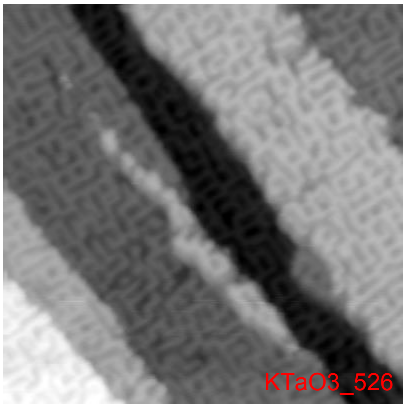

Fig. 12: KTaO$_3$ surface after annealing at 443 K, AFM, 100×100 nm², 3.6 V, 0.004 nA

The large scale STM image (Fig. 12) shows the surface after annealing at 443 K. Compared to the 426 K annealed surface not much difference is visible. The reconstruction is taking place on every terrace. However the lines are not fully oriented yet.

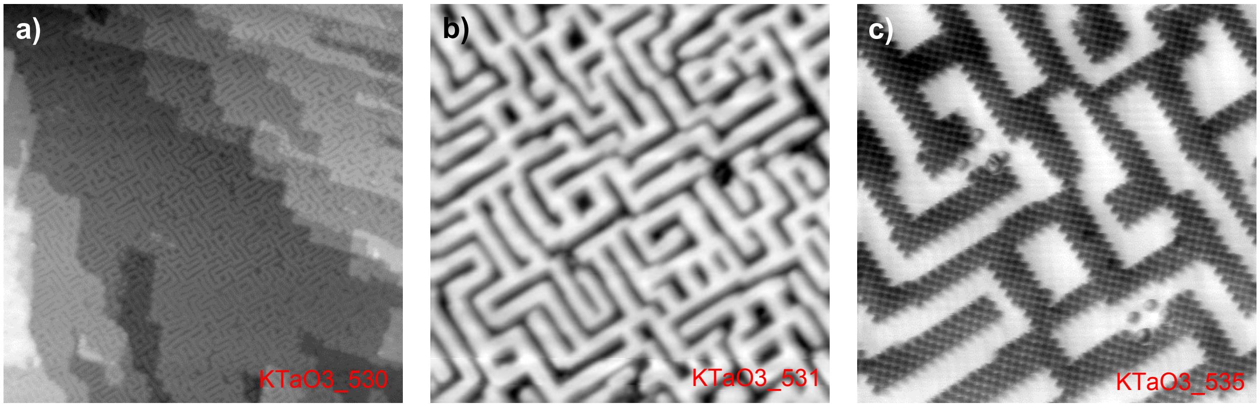

Fig. 13: $KTaO_3$ surface after annealing at 478 K a) STM, 200×200 nm², 3.35 V, 0.006 nA b) STM, 50×50 nm², 3.25 V, 0.006 nA c) AFM, 20×20 nm², 0.02 V

The images in Fig. 13 show the surface after the final annealing step at 478 K. The straight lines have fully arranged along the [110] and [-110] directions. Along the [110] direction the line width is 2-3 unit cells, which corresponds to 4-6 K atoms along the [100] direction. All the samples were annealed using the direct heating method explained in section 3.3.4. Even at liquid helium temperature it was not possible to get resolution on the TaO_2 regions.

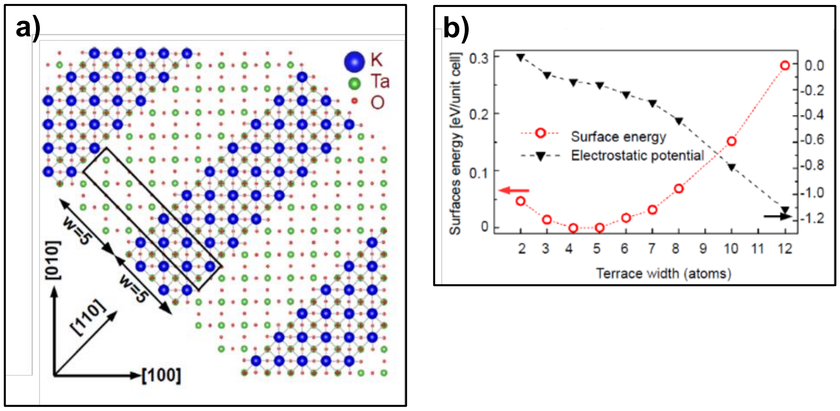

Fig. 14: Results of the DFT calculations carried out by Michele Reticcioli a) model of the annealed surface, the rectangle marks the reconstructed unit cell b) result of DFT calculations of the surface energy for different terrace widths

Fig. 14 a) displays a model of the reconstructed surface. The reconstructed unit cell is marked by the rectangle. From Fig. 14 b) it is apparent that the surface energy reaches its minimum for a line width w of 4-5 atoms, which fits to the experimental results. It is observable that at this step width the electrostatic potential is not at a minimum value. This suggests the consideration that the energy gained by decreasing the electrostatic potential is not high enough to compensate for the step formation energy.

5.2.2 Temperature stability of the labyrinthine structure

The aim of these experiments was to find out up to which temperature the ordered structures that were observed in the previous AFM experiments are stable. To provide a clean surface the sample was cleaved at the beginning and then annealed at temperatures from 423 K to 823 K in steps of 100 K in ultrahigh vacuum. The sample was mounted on a stainless steel sample plate. For the cleaving process the sample was heated to 350 K to achieve a smooth cleavage plane. Between the annealing steps the sample was not cleaved again. To minimize the adsorption of residual gas molecules, the sample was stored in the STM head overnight, where the low temperature and the effective pumping of the cryoshields prevent the surface from being contaminated. The heating was implemented by direct heating on the manipulator, where the sample was annealed for 15 minutes. After annealing the sample was left at room temperature to relax for 10 minutes and then was brought to the STM head, where it was cooled to 78 K and measured afterwards. In the following section the acquired STM images are presented.

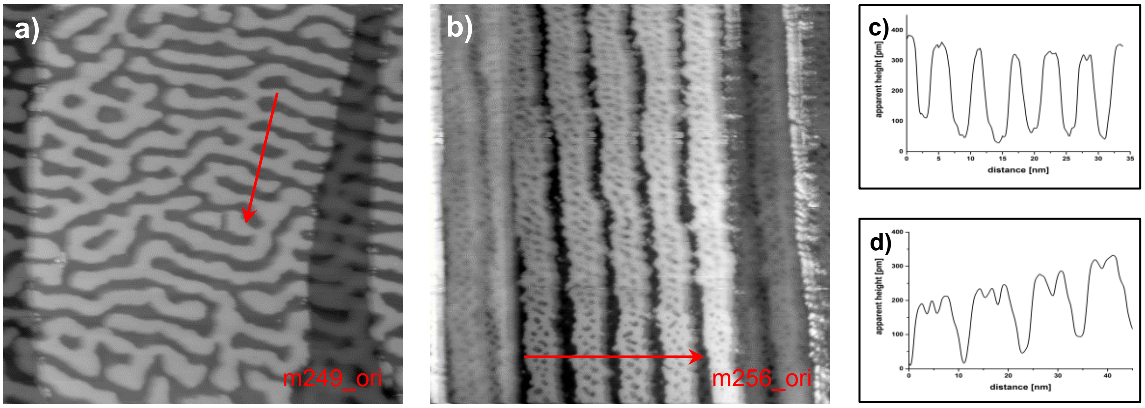

Fig. 15: a) As-cleaved surface, STM, 100×100 nm², 3.5 V, 0.1 nA b) surface after annealing at 423 K, STM, 100×100 nm², 3.5 V, 0.1 nA c) linescan of arrow in (a) d) linescan of arrow in (b)

Fig. 15 shows an image of the as-cleaved (001) surface with the expected polar structure. As in the previous images the brighter areas correspond to the KO surface termination and the darker areas correspond to the TaO_2 termination. The linescan (Fig. 15 c)) reveals that the width of the KO terminated areas is about 5 nm. In Fig. 15 b) an image of the cleaved surface that was annealed at 423 K is displayed. It is recognizable that the surface structure has changed, but does not yet show a specific order. The arrangement in parallel lines of about 10 nm width (see linescan Fig. 15 d)) is probably attributable to the cleavage.

Annealing at 523 K leads to the following images (Fig. 16) and one can see that the surface has further rearranged. The parallel lines have combined to form a grid that extends over the whole surface. It now shows a labyrinthine structure with lines of about 1.5 nm width and a maximum length of about 18 nm from one corner to the next one.

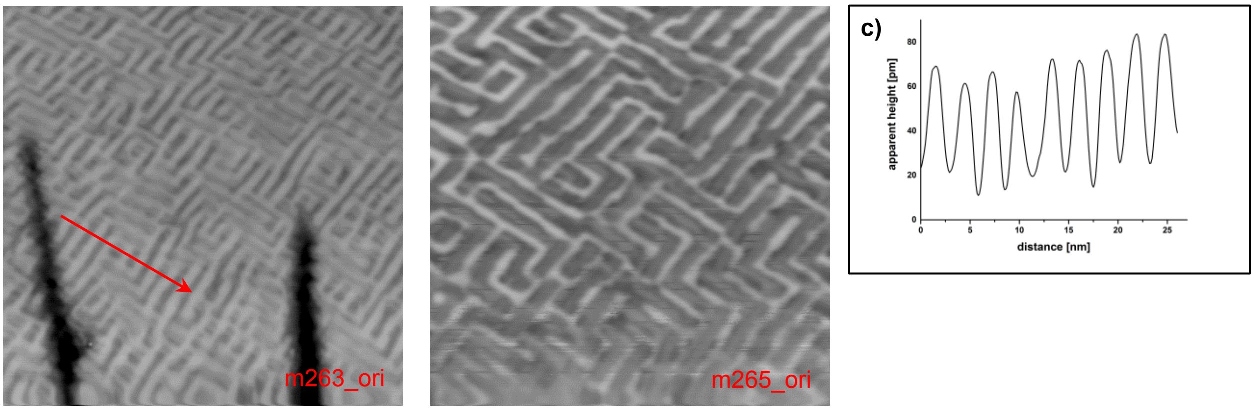

Fig. 16: Surface after annealing at 523 K a) STM, 70×70 nm², 3.2 V, 0.2 nA b) STM, 40×40 nm², 3.2 V, 0.2 nA c) linescan of arrow in a)

After annealing at 623 K still an ordered structure is visible (Fig. 17). Compared to the images of the 523 K annealed surface, the lines become straighter and far more elongated. The length of the longest line that could be measured in Fig. 17 a) is about 53 nm, but larger extensions are certainly possible. As the lines continue across the edges of the imaged area their actual length could not be determined. Along with the increase of the line length the number of corners decreases. The linescan in Figure shows that the line width is still about 1.5 nm. Due to a tip change the edge states of each line are more pronounced now.

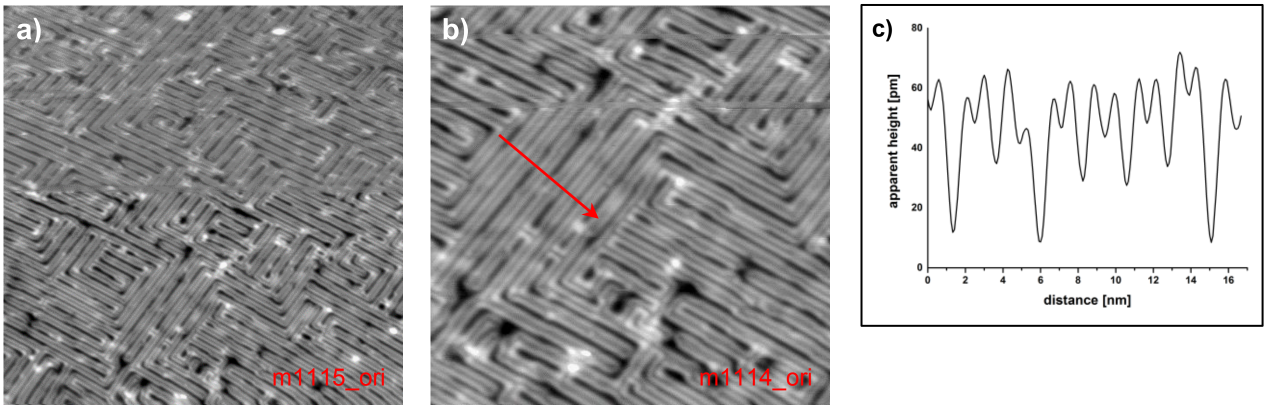

Fig. 17: Surface after annealing at 623 K a) STM, 100×100 nm², 3.35 V, 0.08 nA b) STM, 50×50 nm², 3.35 V, 0.08 nA c) linescan of arrow in b)

Annealing at 723 K (Fig. 18 a)) causes the ordered structure to deform and after annealing at 823 K the ordered structure has completely vanished (see Fig. 18 b) and c)). This may be simply caused by the annealing process but can also be the consequence of residual gas molecules that adsorb during the time between the measurements.

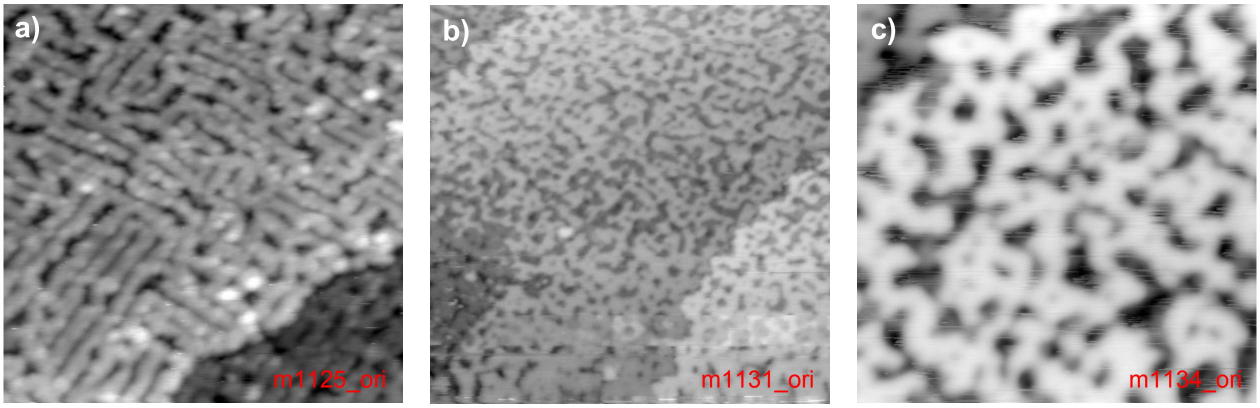

Fig. 18: a) Surface after annealing at 723 K, STM, 50×50 nm², 3.35 V, 0.07 nA b) surface after annealing at 823 K, STM, 100×100 nm², 3.5 V, 0.1 nA c) surface after annealing at, STM, 823 K, 40×40 nm², 3.5 V, 0.1 nA

5.3 Water-induced surface restructuring

5.3.1 Dosing 100 L H_2O at room temperature

The sample was cleaved at room temperature and 100 L H_2O were dosed onto the surface at room temperature. In Fig. 19 the resulting images are depicted.

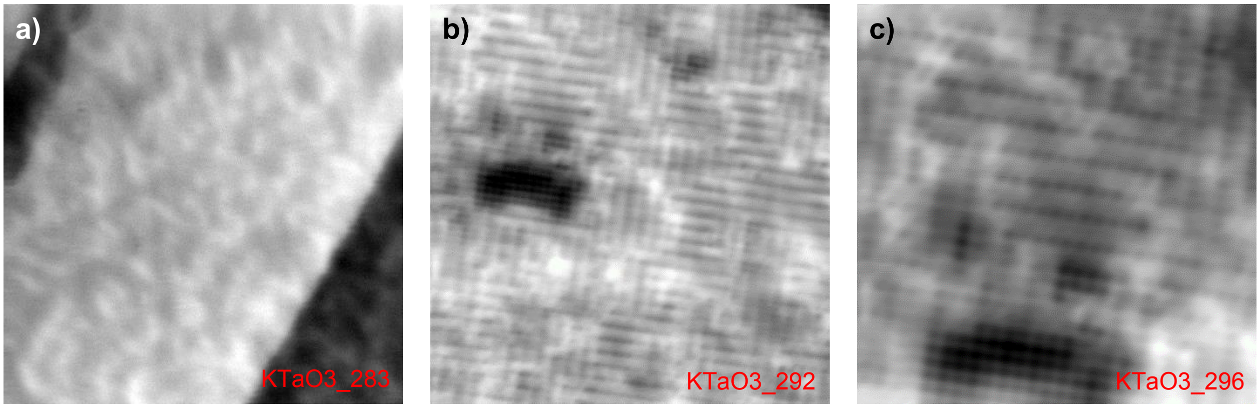

Fig. 19: $KTaO_3$ surface after 100 L H_2O dosage a) AFM, 200×200 nm², 1.0 V, -1.6 Hz b) AFM, 20×20 nm², 0.001 V c) AFM, 10×10 nm², 0.001 V

One can see that the original polar surface has completely vanished and ordered lines have taken its place. The small scale images (Fig. 19 b) and c)) show only small regions of the KO termination. This indicates that the surface is dissolved and a new structure is formed by the H_2O molecules that are bound to the surface. It is also clear that the TaO_2 terminated regions are covered first.

5.3.2 Dosing 300 L of H_2O at room temperature

Additional to the 100 L of H_2O that were dosed onto the sample in the previous experiment another 200 L of H_2O were dosed at a temperature of 321 K. In Fig. 20 the corresponding images are displayed.

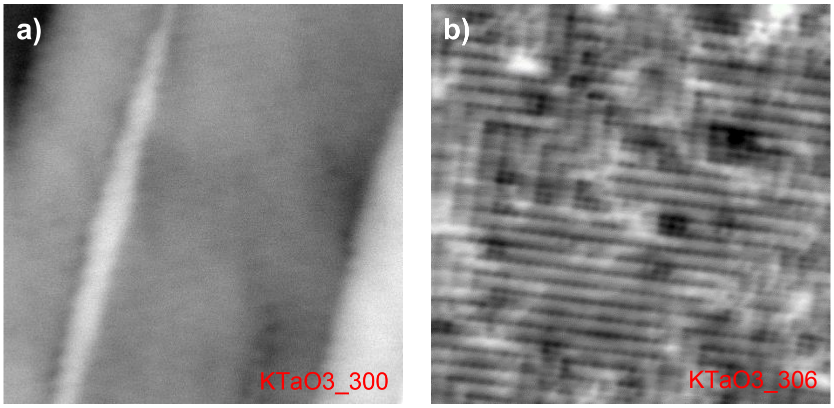

Fig. 20: $KTaO_3$ surface after 300 L H_2O dosage a) AFM, 80×80 nm², 0.01 V, -0.7 Hz b) AFM, 15×15 nm², 0.01 V

On the large scale the surface now looks even smoother compared to the measurements with 100 L H_2O. The smaller scale image reveals that the surface is almost completely dissolved by the H_2O molecules. Also the domains with parallel lines become larger.

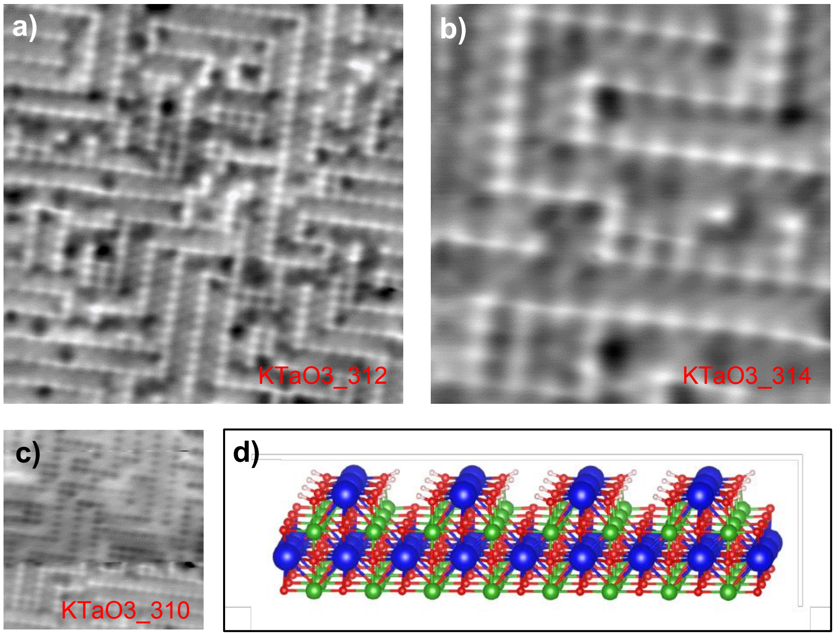

Fig. 21: $KTaO_3$ surface after 300 L H_2O dosage a) AFM, 10×10 nm², 0.01 V b) AFM, 4×4 nm², 0.01 V c) AFM, 7.5×7.5 nm², 0.01 V d) model of the (2×1) reconstructed surface with hydroxyl groups, provided by Michele Reticcioli

Fig. 21 shows images of the same surface but with a different contrast. The reason for that is an alteration of the tip, which can occur because of an atom sticking to the tip apex and thereby changing its behavior. In this way it is possible to image different sorts of atoms. Fig. 21 a) exhibits the transition between the two different states of the tip. The bright dots in Fig. 21 are situated at the areas that could not be resolved in the previous images. In both cases the K atoms are imaged but in one case the tip senses an attractive force and in the other case the force is repulsive.

It appears that the KO units that previously were bound together in islands now are distributed all over the TaO_2 layer. To each of these KO units one H_2O molecule is bound resulting in a (2×1) reconstruction of consisting of $K(OH)_2$ units (see Fig. 21 d)). This model is supported by results from XPS and LEIS measurements that are presented in sections 6.2 and 7.1.2 respectively. The reconstructed surface has a charge of -0.5 e per (1×1) unit cell, which implies a polarity compensation, this time by chemical bonding to adsorbates.

5.4 Water adsorption in the sub-monolayer regime

5.4.1 Dosing 1 L of H_2O and annealing at room temperature

For these experiments the sample was cleaved at room temperature. Then the sample was cooled to 97 K with liquid nitrogen, and 1 L of H_2O was dosed on the surface by applying a pressure of 2×10^{-8} mbar H_2O for 80 seconds. After this preparation the sample was scanned in STM and AFM mode at 78 K. To allow for a relaxation of the surface, the sample was annealed at room temperature for 15 minutes and measured again. The following images (Fig. 22) show a comparison between the as-dosed and the dosed and annealed surface.

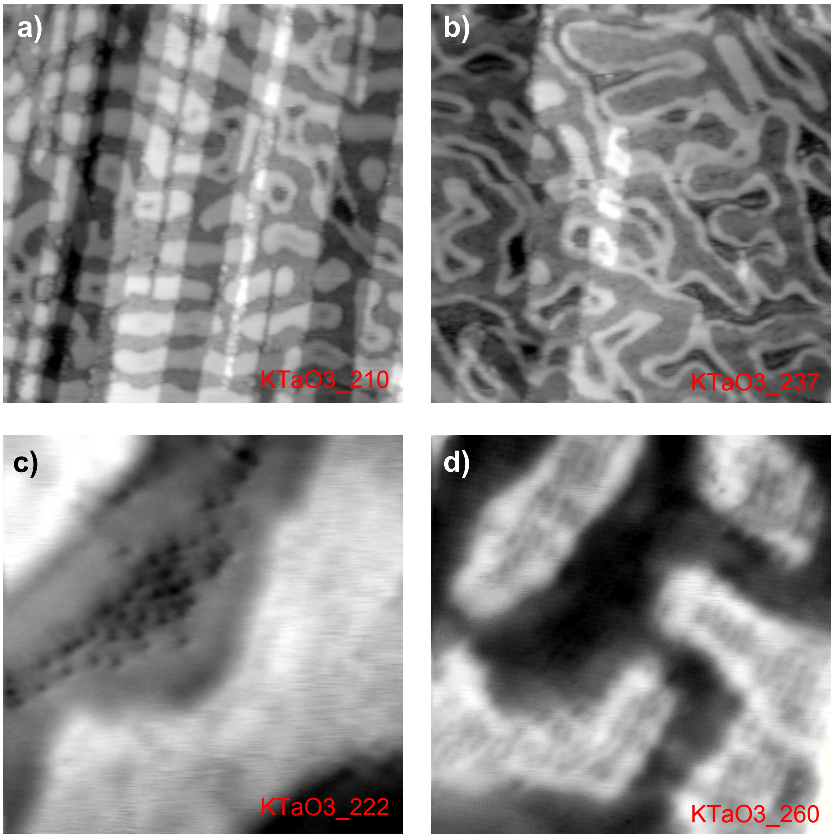

Fig. 22: a) $KTaO_3$ surface after 1 L H_2O dosage at 97 K, STM, 100×100 nm, 3.2 V, 0.005 nA b) $KTaO_3$ surface after 1 L H_2O dosage at 97 K and annealing at room temperature, STM, 100×100 nm², 3.0 V, 0.005 nA c) $KTaO_3$ surface after 1 L H_2O dosage at 97 K, AFM, 16×16 nm², 0.0001 V d) $KTaO_3$ surface after 1 L H_2O dosage at 97 K and annealing at room temperature, AFM, 25×25 nm², 0.0001 V

Fig. 22 shows test experiments with adsorption of submonolayer water coverages. Dosing water vapor at 97 K indicates molecular adsorption, where the molecules are highly mobile at the TaO_2 terrace (Fig. 22 a) even at the measurement temperature of 78 K. Annealing results in stabilization of the surface and an ordered adsorption pattern is found on the TaO_2 terraces (Fig. 22 d). Water adsorption is accompanied with significant changes in the surface electronic structure (Fig. 22 a, b)

5.4.2 Dosing 300 L water vapor and annealing at up to 523 K

To determine the temperature stability of the (2×1) reconstruction STM measurements were performed on a cleaved and an H_2O dosed surface. The cleavage was carried out at a sample temperature of 368 K. After the H_2O dosage the sample was annealed at 373 K, 473 K and 523 K and investigated in STM after each heating step. Again the heating was implemented via direct heating on the manipulator. The sample was annealed for 15 minutes at the respective temperature and left at room temperature for 10 minutes to relax before it was inserted into the STM head.

Before the H_2O dosage again the as-cleaved surface was scanned to ensure that the expected polar structure was present at the surface (Fig. 23 a)). Thereby one can see that the surface is not as flat and the step edges are not as straight as in the previous measurements. This can occur due to irregularities in the crystal growth, slight differences in the cleaving angle or because of the higher sample temperature during the cleaving procedure. Apart from this the surface shows the expected structure.

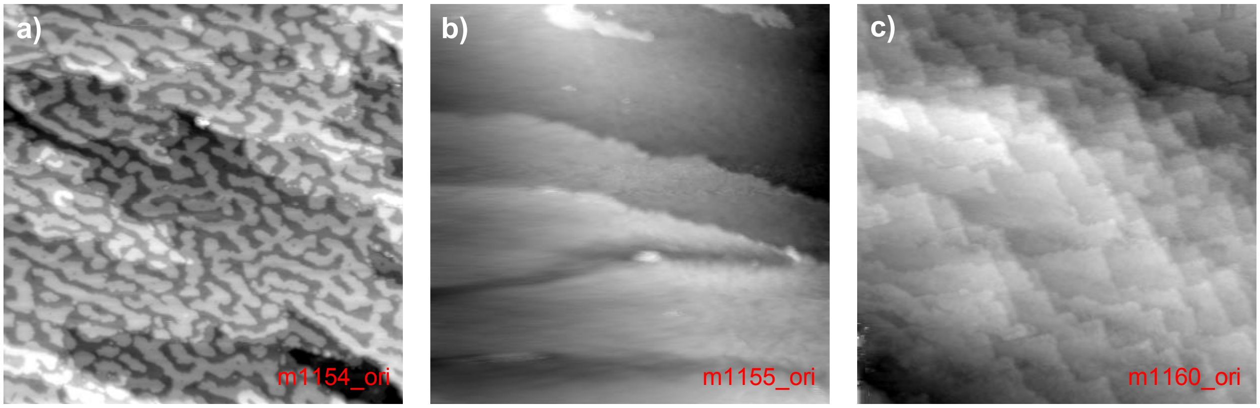

Fig. 23: a) As-cleaved surface, STM, 100×100 nm², 3.5 V, 0.1 nA b) surface after 300 L H_2O dosage, STM, 100×100 nm², 3.5 V, 0.1 nA c) surface after 300 L H_2O dosage, STM, 100×100 nm², 3.3 V, 0.07 nA

After dosing 300 L H_2O no structure is visible at the terraces. In Fig. 23 b) and c) the resulting images are displayed. The images were acquired at different positions on the cleavage plane. Unfortunately it was difficult to image the water dosed surface because water molecules stuck to the tip. This caused diffuse images and multiple tip imaging artifacts. On the other hand qualitative information about the bond strength between the H_2O molecules and the surface atoms was gained. Apparently the H_2O molecules are only weakly bound to the crystal surface. It should be noted that at the most-stepped regions of the surface, the H_2O dosage leads to straight step edges and rectangular corners.

Annealing the H_2O dosed surface at 373 K surface leads to the following structure (Fig. 24). Again the images are acquired at different positions on the cleavage plane. Small clusters are visible that may be formed by water molecules or hydroxyl groups.

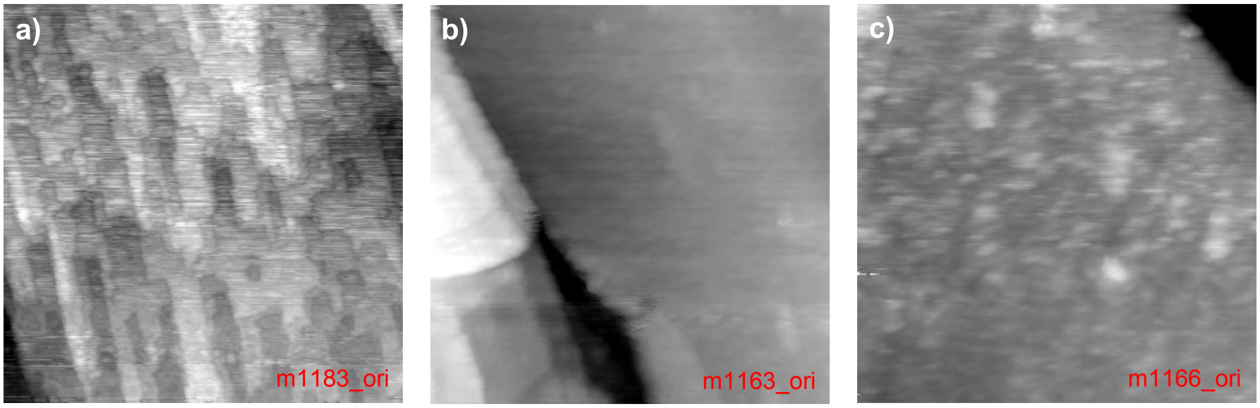

Fig. 24: Surface after 300 L H_2O dosage and annealing at 373 K a) STM, 100×100 nm², 2.1 V, 0.1 nA b) STM, 100×100 nm², 3.3 V, 0.07 nA c) STM, 50×50 nm², 3.3 V, 0.07 nA

Further annealing at 473 K leads to the images presented in Fig. 25 a) and b). One can see clear structures that resemble the structures measured on the cleaved surface after annealing at 523 K. The step edges are straight with rectangular corners. Another annealing step at 523 K was done on the H_2O dosed surface to achieve comparable temperatures (see Fig. 25 c)).

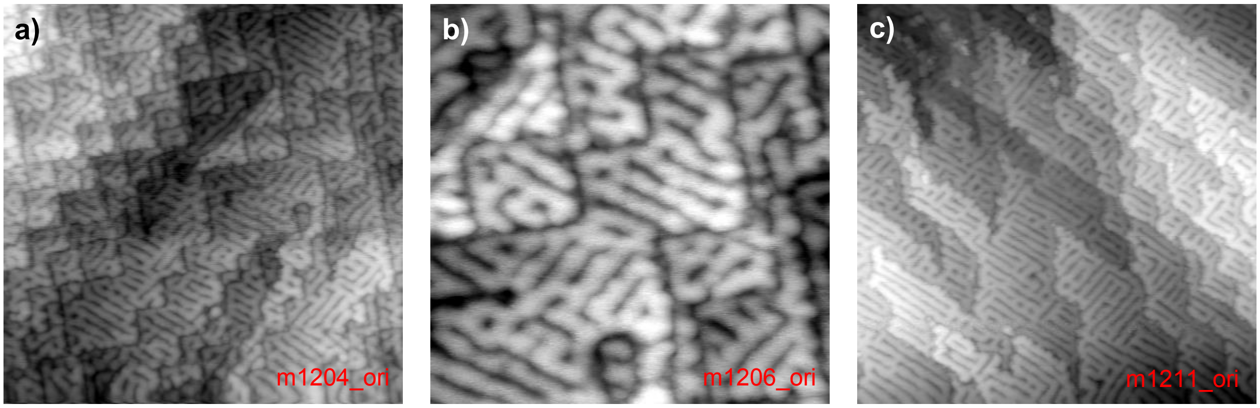

Fig. 25: a) Surface after 300 L H_2O dosage and annealing at 473 K, STM, 100×100 nm², 3.3 V, 0.1 nA b) surface after 300 L H_2O dosage and annealing at 473 K, STM, 40×40 nm², 3.3 V, 0.1 nA c) surface after 300 L H_2O dosage and annealing at 523 K, STM, 100×100 nm², 3.3 V, 0.1 nA

Compared to annealing at 473 K the lines are more elongated after annealing at 523 K, which may be because of the higher annealing temperature or simply depend on the position on the cleavage plane.

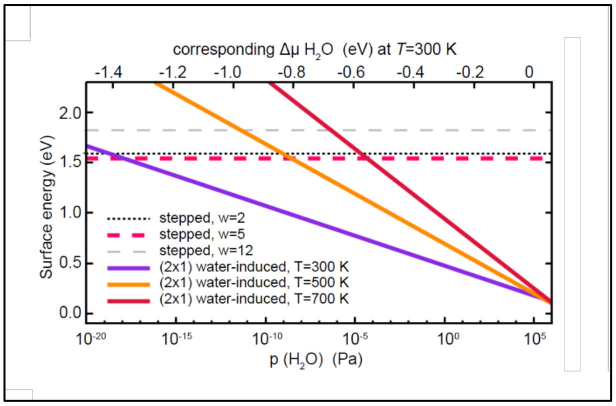

Fig. 26: DFT calculated phase diagrams for several annealing temperatures provided by Michele Reticcioli

The stability of the (2×1) reconstruction was investigated by DFT methods via calculation of the surface energy as a function of the H_2O partial pressure or the change in the chemical potential (see Fig. 26). At room temperature the reconstructed surface is stable even for extremely low partial pressures of 10^{-18} Pa. An annealing temperature of 500 K still allows for a stable (2×1) reconstruction in the range of H_2O partial pressures between 10^{-9} and 10^{-5} Pa. This is consistent with the experimental results that show a transition between the (2×1) reconstructed and the stepped surface at an annealing temperature of 523 K. Higher annealing temperatures would require higher amounts of water vapor to stabilize the (2×1) reconstruction.

5.5 Annealing after electron bombardment

Another cycle of STM measurements was performed on a cleaved and annealed $KTaO_3$ surface with a few experimental modifications. The sample was now mounted on a Ta sample plate, because that allows heating up to higher temperatures as compared to stainless steel. Degassing was done via electron bombardment at a temperature of 983 K for about one hour. The sample was cleaved at room temperature and immediately annealed at 723 K via electron bombardment. Heating to the final annealing temperature was extended to a duration of about 30 minutes, and the same time was spent to slowly cool the sample to room temperature before it was transferred to the STM head. The resulting image is displayed in Fig. 27 a). To exclude influences of the heating method a similar experiment was performed using direct heating. Therefore the sample was cleaved again, annealed at 423 K and finally annealed at 673 K.

Fig. 27 a) shows the cleaved surface after annealing at 723 K via electron bombardment. Apparently there is no ordered structure that one could have expected considering the previous measurements. Electron bombardment is likely to be the reason for that. To avoid the influence of the electron bombardment the sample was cleaved again and the annealing steps were carried out via direct heating. Fig. 27 b) shows the surface after annealing at 423 K via direct heating. As in the previous experiments the ordered structure could be detected. Still it should be noted that the cleavage plane does not look as smooth as in the previous measurements. Many small islands are present on top of the ordered structure, which can be caused by crystal defects or by small inaccuracies in the cleaving process.

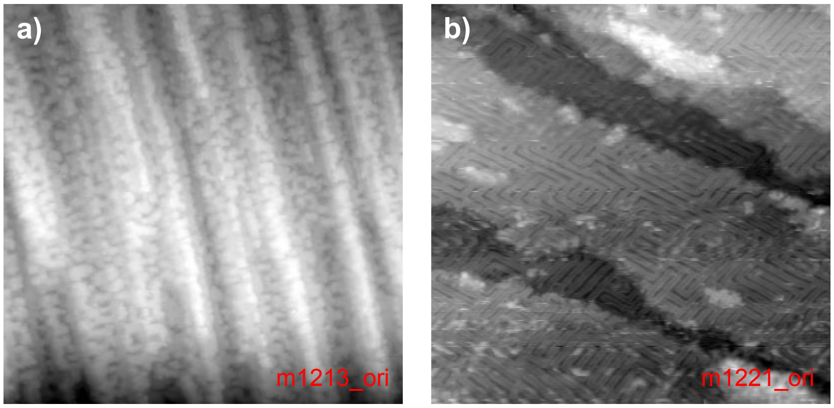

Fig. 27: a) Surface after annealing at 723 K via electron bombardment, 100×100 nm², 3.5 V, 0.1 nA b) surface after annealing at 423 K via direct heating, 100×100 nm², 3.3 V, 0.1 nA

The sample was then annealed at 673 K via direct heating and the resulting images are presented in Fig. 28. Thereby different features can be observed. On the one hand the step edges are straight with rectangular corners, on the other hand the structure on the terraces is not ordered at all. Also there is an additional type of surface structure that was not observed in the previous measurements.

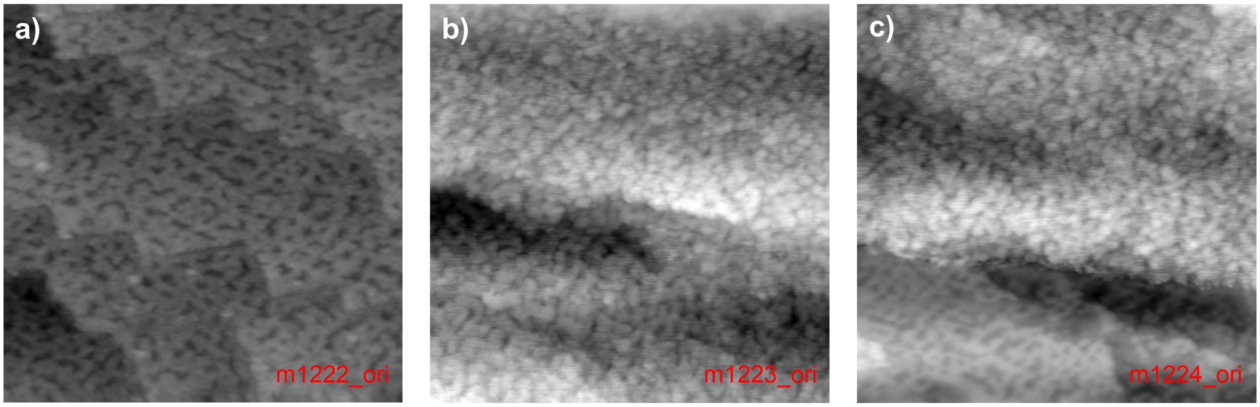

Fig. 28: a) Surface after annealing at 673 K via direct heating, 80×80, 3.3 V, 0.1 nA b) surface after annealing at 673 K via direct heating, 100×100, 3.3 V, 0.1 nA c) surface after annealing at 673 via direct heating, 100×100, 3.3 V, 0.1 nA

The images obtained in these measurements seem surprising because they differ from the previous measurements. After annealing at the same temperatures different surface structures were detected. This may be due to several reasons. One possibility is that the reconstructions depend on the quality of the cleavage plane. On much stepped areas an ordered structure is formed less easily, while a smooth and even cleavage plane should facilitate the formation of an ordered surface reconstruction. Also the surface could be contaminated by residual gas molecules that adsorb at a certain temperature. Another explanation is that the sample was outgassed at 983 K, which results in the loss of oxygen from the bulk. This may change the polarity-compensation.

6 XPS measurements

6.1 Measurement procedure

The samples that were investigated in the XPS measurements were degassed via direct heating on the manipulator at 873 K. Prior to each measurement cycle the sample was cleaved and the required amount of water was dosed onto the surface. For the fixation of the sample a stainless steel sample holder was used to avoid an overlap of the Ta signals from the crystal and the sample holder. All the experiments were carried out with grazing incidence of the X-rays and normal exit of the detected photoelectrons, which implies an angle of 65° between the X-rays and the surface normal. For all the measurements a magnesium anode with an excitation energy of 1253.6 eV was applied. The overview spectra were acquired with a pass energy of 20 eV, a step width of 1 eV and a dwell time of 0.05 s. In order to receive a better resolution, the detailed spectra were measured with a pass energy of 10 eV, a step width of 0.1 eV, and a dwell time of 0.2 s. The spectra of the H_2O dosed surface were normalized to the minimum value of the as-cleaved spectrum.

6.2 Results and discussion of the XPS measurements

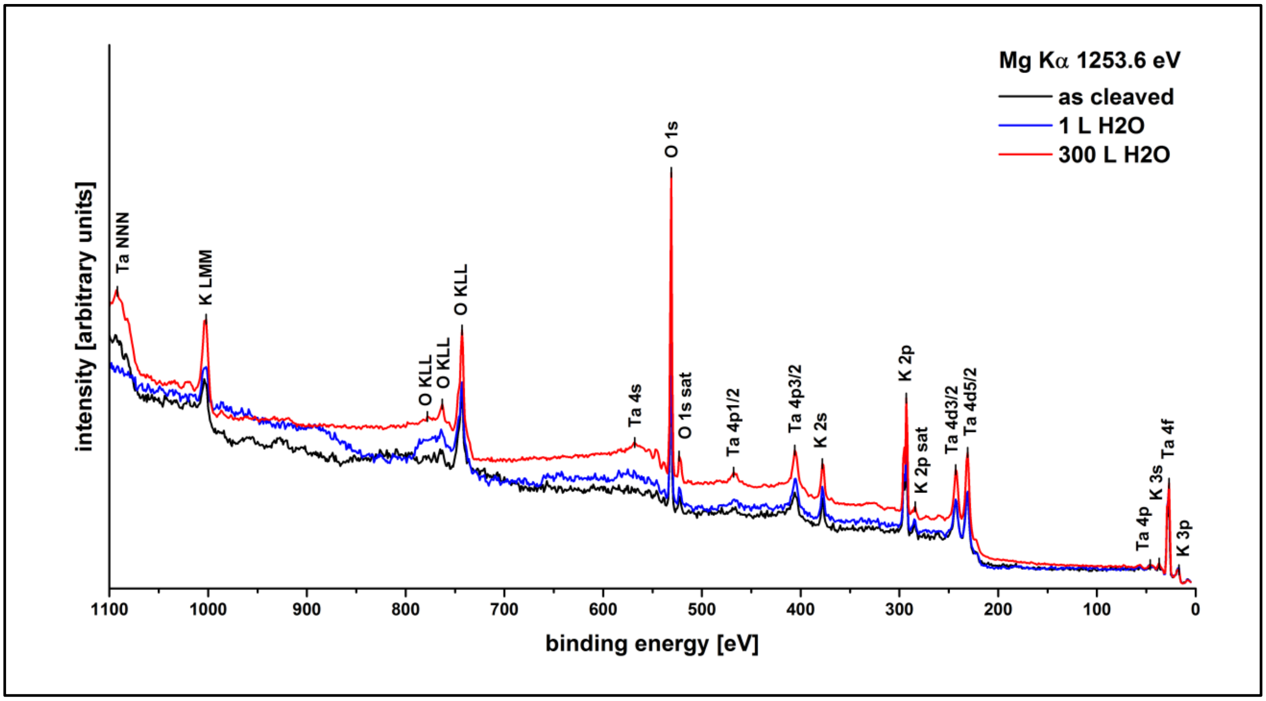

Fig. 29: XPS spectra of an as-cleaved surface and after H_2O dosages of 1 L and 300 L

Fig. 29 shows the XPS spectra of an as-cleaved surface, a cleaved surface with a water dosage of 1 L and a cleaved surface with a water dosage of 300 L. The data were acquired from different samples that had the same doping but different sizes and slightly different shapes. It was therefore not possible to achieve exactly the same measurement conditions. That is why the intensities cannot be compared quantitatively. What can be learned from these spectra is that the sample mainly consists of K, Ta and O. The signal of the dopant elements is too small to be distinguished from the background signal. Also there is no significant contamination from sample impurities, residual gas molecules, or the sample plate.

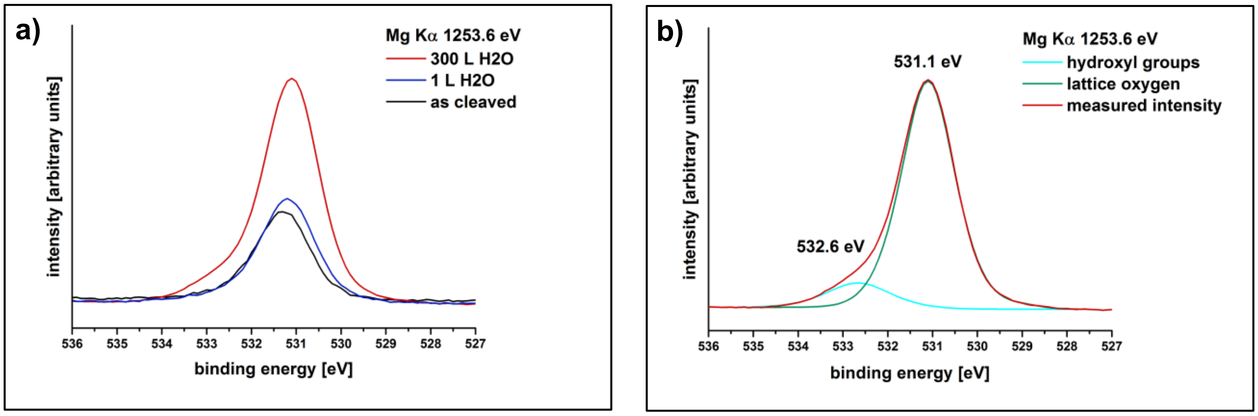

Fig. 30: a) XPS spectra the O 1s peak of an as-cleaved surface and after H_2O dosages of 1L and 300 L b) peak fit of the 300 L H_2O spectrum in (a)

In Fig. 30 a) the O 1s peak is presented for different H_2O dosages. It is clearly visible a shoulder appears at the left side of the peak in the spectrum of the 300 L H_2O dosed surface. This is due to hydroxyl groups that are formed at the surface after the H_2O dosage. Fig. 30 b) shows a peak fit of the O 1s peak after 300 L H_2O dosage that contains the hydroxyl shoulder. The CasaXPS© processing software was used for the peak fit. For the line shape the product of a Gaussian with a Lorentzian function was applied. The position of the lattice oxygen peak is at 531.1 eV, while the position of the hydroxyl peak is at 532.6 eV.

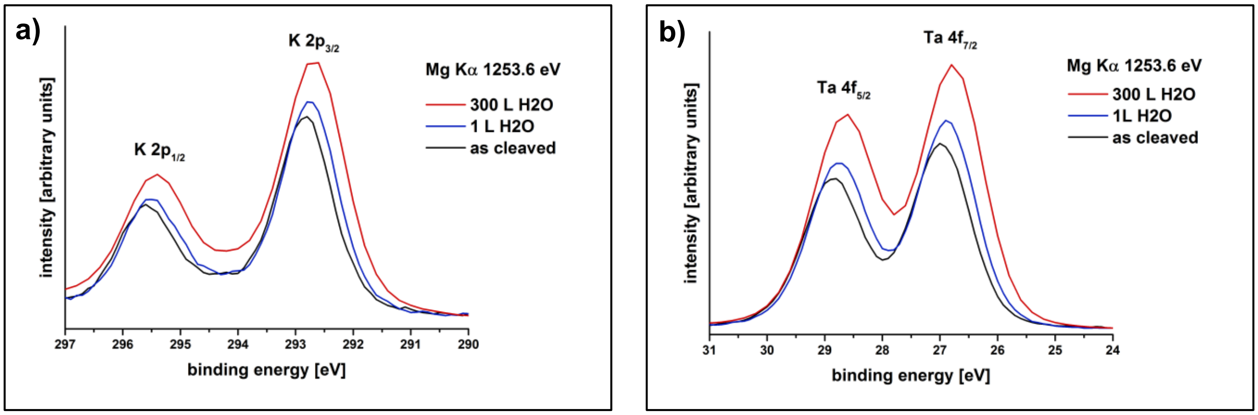

Fig. 31: XPS spectra of an as-cleaved surface and after H_2O dosages of 1L and 300 L of the a) K 2p and b) Ta 4f core level peaks

In Fig. 31 the detailed spectra of the core level peaks of K and Ta are displayed. Compared to the elemental core levels (see [51]) the K peaks (K $2p_{1/2}$ at 295.6 eV, K $2p_{3/2}$ at 292.8 eV) are shifted by about 1 eV towards lower binding energy. The Ta $4f_{5/2}$ and Ta $4f_{7/2}$ core level peaks are situated at 28.9 eV and 27 eV respectively, which are common values for tantalum oxides [65]. All the detailed spectra show a peak shift of about 0.2 eV towards lower binding energies between the as-cleaved and the 300 L H_2O dosed surface. This is probably due to band bending effects that are caused by the local imbalance in charge neutrality at the cleaved surface. For better clarity the peak positions of the detailed spectra are listed in Table 1.

	binding energy [eV]				
	O 1s	K $2p_{1/2}$	K $2p_{3/2}$	Ta $4f_{5/2}$	Ta $4f_{7/2}$
as-cleaved	531.3	295.6	292.8	28.9	27.0
1 L H_2O	531.2	295.5	292.7	28.8	26.9
300 L H_2O	531.1	295.4	292.6	28.6	26.8

Table 1: Peak positions of the O, K and Ta core level peaks on the cleaved and H_2O dosed $KTaO_3$ surface.

7 LEIS measurements

Because the surface is damaged easily by the impinging ions it is important to optimize the sample position quickly and perform the measurement soon after sample preparation. Residual gas molecules start to adsorb at the surface which causes a higher background signal and additional peaks in the spectra. The measurements were carried out in about 4.5×10^{-8} mbar helium and an ion acceleration voltage of 1 kV was applied. Normal incidence of the ions was chosen to avoid contributions from the lateral sample surface and achieve high surface sensitivity.

7.1 Dosing H_2O onto an as-cleaved surface

7.1.1 Measurement procedure

The sample was cleaved and analyzed with LEIS in normal incidence and grazing exit with an angle of 45° between the surface normal and the analyzer entrance. Then the sample was cleaved again and 300 L H_2O were dosed onto the surface straight after the cleaving process. A pass energy of 100 eV, a step width of 1 eV and a dwell time of 0.2 s were applied. The H_2O dosed surface was measured with the classical focusing method where the sample is measured in fixed energy mode and is moved until the intensity is at its maximum. For the water-induced surface the classical focusing method was applied, while for the as-cleaved spectrum the focusing is carried out via the STM scanning software (see 4.5.2).

7.1.2 Results and discussion

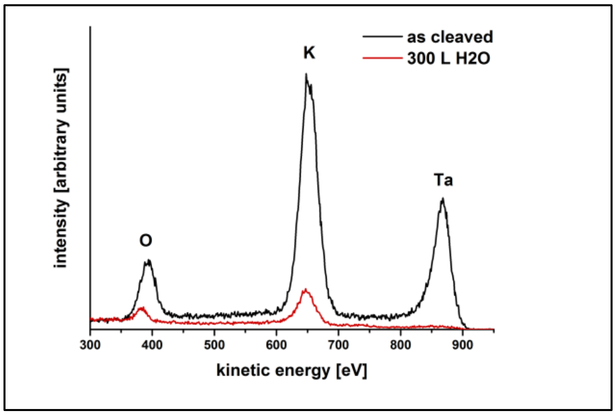

Fig. 32: LEIS spectra of an as cleaved $KTaO_3$ surface and an as cleaved surface after an H_2O dosage of 300 L

Fig. 32 shows LEIS spectra of an as-cleaved surface and a surface that was cleaved and dosed with 300 L H_2O. It is clearly recognizable that the Ta peak has vanished after the H_2O dosage. This fits to the model where the $KTaO_3$ surface is dissolved and the TaO_2 layers are completely covered by potassium atoms and hydroxyl groups. The peak maxima of the oxygen peak are shifted by about 10 eV. This can be attributed to the additional energy loss due to scattering of the He ions at the protons of the hydroxylated surface. For both measurements the same sample is used. The difference in the intensities can on one hand be derived from the H_2O dosage but on the other hand is caused by the use of different focusing methods.

7.2 Dosing H_2O without intermediate cleaving

7.2.1 Measurement procedure

This experiment is discussed to emphasize the importance of short ion bombardment times to avoid sample damage. Here the sample was cleaved only once prior to the acquisition of the as-cleaved spectrum. H_2O was dosed onto the surface that had already been analyzed, i.e. bombarded with ions. A pass energy of 110 eV, a step width of 1 eV and a dwell time of 0.1 s were used. To focus the ions the scanning software was applied again.

7.2.2 Results and discussion

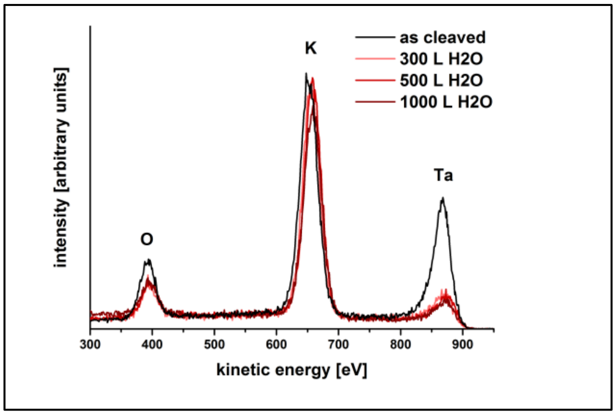

Fig. 33: LEIS spectra of an as cleaved $KTaO_3$ surface and after dosing H_2O onto the ion bombarded surface

Fig. 33 shows the LEIS spectra of an as-cleaved surface and of an ion bombarded surface that was dosed with different amounts of water. Compared to the previous LEIS measurements it is remarkable that the Ta peak does not vanish completely, although much higher amounts of H_2O are dosed. With the first H_2O dosage the intensity of the Ta peak and the O peak decreases, but any further H_2O dosage does not change the signal significantly. This shows that the surface is damaged by the impinging ions and H_2O molecules can only partially adsorb on the analyzed surface. As a consequence it is important to prepare the sample prior to each experiment and to perform the measurements within a short time range.

8 LEED measurements

8.1 Results and discussion of the LEED measurements

LEED measurements were performed to determine the structure and the stability of the annealed and the water-exposed surface. Several experiments were performed and the resulting LEED patterns are shown in the figures below.

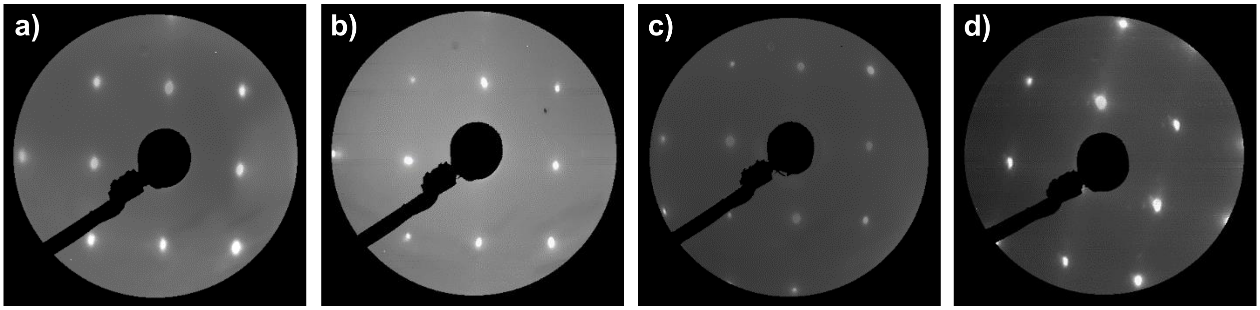

Fig. 34: LEED patterns of the a) as cleaved surface b) the surface after annealing at 588 K c) after annealing at 588 K and dosing 1 L of water vapor and d) after dosing 300 L H_2O, annealing at 523 K and dosing another 300 L H_2O

In Fig. 34 a) the LEED pattern of an as-cleaved surface is depicted and the expected square symmetry of the bulk crystal is visible. Fig. 34 b) shows the LEED pattern after cleaving and annealing at 588 K. Considering the results from the STM experiments, an ordered superstructure could have been expected. Nevertheless there is only the bulk signal. Dosing 1 L of water vapor onto the 588 K annealed surface does not cause any change in the pattern (Fig. 34 c)). For the pattern in Fig. 34 d) 300 L of water vapor are dosed onto the cleaved surface and the sample is annealed at 523 K. To check if H_2O molecules still stick to the surface after annealing another 300 L of water vapor were dosed onto the annealed surface. The LEED pattern does not show any reconstructions, which points out that H_2O molecules do not adsorb on the reconstructed surface (Fig. 34 d)).

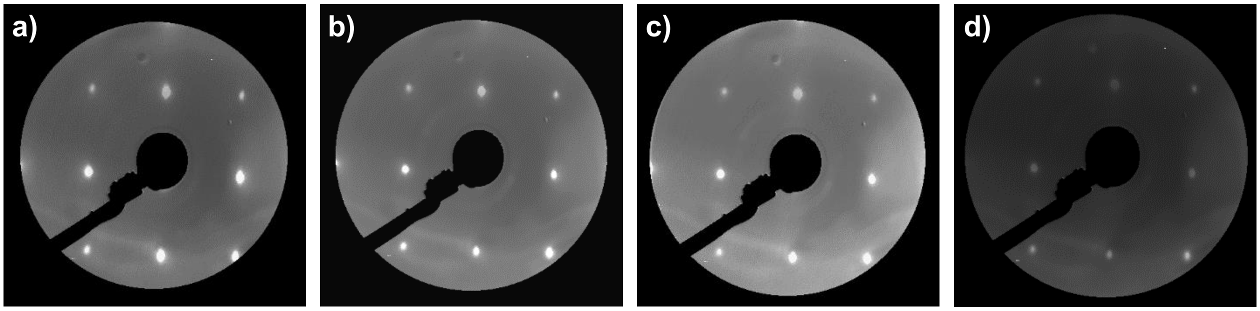

Fig. 35: LEED patterns of the cleaved surface after annealing at a) 300 K b) 500 K c) 700 K and d) 885 K

Fig. 35 shows the patterns of another set of annealing steps. The sample was therefore slowly heated and LEED patterns were acquired during the heating procedure. Again no change in the pattern due to annealing is visible. The fact that no change in the surface structure can be detected by LEED may be ascribed to the electron bombardment, which probably prevents the formation of ordered reconstructions on $KTaO_3$. It should also be noted that the LEED measurements were performed on a surface that had been investigated with LEIS before. The sample damage caused by the He ions may as well be a factor that inhibits ordered reconstructions.

Finally a (2×1) reconstruction can be observed (Fig. 36) after dosing 300 L of water vapor onto an as-cleaved surface and performing the LEED measurement straight after the H_2O dosage.

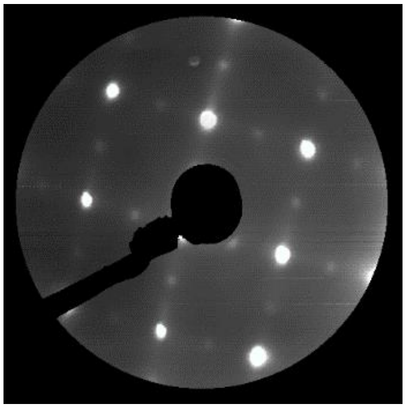

Fig. 36: LEED pattern of cleaved surface after dosing 300 L of water vapor; the (2×1) structure is clearly visible.

The additional diffraction spots provide an evidence for the (2×1) reconstruction that appears on the surface after water dosage. It should be mentioned that the diffraction pattern of the reconstructions was only visible for about 10 seconds and vanished afterwards. This tells that electron bombardment is highly destructive for the water-induced surface.

9 Conclusion

Cleaving $KTaO_3$ single crystals in UHV leads to a polar surface consisting of regions with a KO termination and regions with a TaO_2 termination, whereby the area percentage of both terminations equal. The shape of these regions does not show a specific symmetry and the KO layer is always on top of the TaO_2 layer. The height difference between the KO and the TaO_2 terminated regions is half a unit cell. With STM it is not possible to achieve atomic resolution on $KTaO_3$. AFM provides atomic resolution on the KO termination, the TaO_2 termination still cannot be atomically resolved. LEIS and XPS results show that the surface is clean and no impurity atoms appear at the cleaved surface. LEED shows the expected square symmetry.

Annealing of the cleaved surface causes reconstructions that lead to straight lines along the [110] direction. The reconstructed surface still consists of KO terminated regions on top of a TaO_2 termination and also their ratio stays the same. This indicates that the surface reconstruction mechanism is based on surface diffusion. It is evident from the AFM images that the line width along the [110] direction is two unit cells and four K atoms along the [100] direction. The reconstructions start with annealing at 371 K and reach an ordered structure after annealing at about 478 K. According to both the experiments and the DFT calculations, step widths of 4-5 atoms are energetically favorable. With increasing temperature the lines become straighter and longer with a lower number of corners. This labyrinthine structure stays stable for annealing temperatures up to 723 K, where the order starts to break. After annealing at 823 K the surface is completely disordered again.

Dosing H_2O onto the as-cleaved surface leads to a (2×1) reconstruction that dissolves the polar surface. With increasing amounts of H_2O the TaO_2 regions are covered first and then the KO regions are dissolved. A dosage of 300 L H_2O leads to a completely reconstructed surface. At low temperatures, such as 97 K, H_2O molecules diffuse at the surface but do not dissociate. Room temperature is sufficient for the H_2O molecules to bind to the surface and form the (2×1) reconstruction. Here the polarity is compensated by the adsorption of H_2O molecules. AFM provides atomic resolution on the water induced surface, while STM images do not exhibit any resolved structure. LEIS measurements prove that the TaO_2 termination is covered first. XPS shows that the H_2O molecules are adsorbed as hydroxyl groups and the (2×1) reconstruction can be confirmed by LEED. DFT calculations suggest a stable reconstruction for temperatures up to 500 K, which is consistent with the experiment. Higher temperatures cause the H_2O to desorb again and the labyrinthine structure reforms.

Measurements implemented on a sample that was degassed via electron bombardment show a different behavior regarding the temperature stability, which reveals the influence of the sample preparation method. It is found that $KTaO_3$ is very sensitive to bombardment with electrons and ions, which implies a certain importance for short timed measurements and sample preparation prior to each experiment.

10 Abbreviations

AFM	atomic force microscopy
nc-AFM	non-contact atomic force microscopy
STM	scanning tunneling microscopy
LEIS	low energy ion spectroscopy
XPS	X-ray photoelectron spectroscopy
LEED	low energy electron diffraction
SPA-LEED	spot profile low energy electron diffraction
PEC	photoelectrochemical
2DEG	two dimensional electron gas
IMFP	inelastic mean free path
LDOS	local density of states
FWHM	full width at half maximum
STS	scanning tunneling spectroscopy
DFT	density functional theory
L	Langmuir
UHV	ultrahigh vacuum

Table of Figures

Fig. 1: a) perovskite structure of $KTaO_3$ b) sketch of cleavage plane c) KO termination d) TaO_2 termination 5

Fig. 2: a) doped $KTaO_3$ single crystals b) cleaved $KTaO_3$ surface 6

Fig. 3: a) cleaving stage in the qPlus chamber b) cleaving stage in the LT-STM chamber c) sample holder 7

Fig. 4: Schematic of an STM instrument 9

Fig. 5: Lennard-Jones potential, where r is the tip-sample distance and ε is the depth of the potential well. At rm the potential is zero and at req the total force is zero. 13

Fig. 6: a) schematic of an X-ray source with twin anodes based on [53] b) schematic of hemispherical analyzer based on [27] 17

Fig. 7: Schematic for the definition of the scattering angle θ and the incident angle α. 18

Fig. 8: a) Schematic of a LEED apparatus based on [60] b) picture of LEED instrument (1) and coil (2) 20

Fig. 9: a) cleaved at room temperature, STM, 100×100 nm², 3.0 V, 0.01 nA b) cleaved at 350 K, STM, 100×100 nm², 3.5 V, 0.1 nA c) cleaved at room temperature, STM, 25×25 nm², 3.0 V, 0.01 nA d) cleaved at room temperature, AFM, 5×5 nm², 0.45 V 21

Fig. 10: a) as cleaved surface, AFM, 17×17 nm², -0.2 V b) surface after annealing at 371 K, AFM, 18×18 nm², -0.5 V c) surface after annealing at 387 K, STM, 60×60 nm², 3.2 V, 0.002 nA d) surface after annealing at 387 K, AFM, 18×18 nm², 0.1 V 22

Fig. 11: $KTaO_3$ surface after annealing at 426 K a) AFM, 100×100 nm², 0.001 V, -1.8 Hz b) AFM, 16×16 nm², 0.001 V c) AFM, 10×10 nm², 0.001 V 23

Fig. 12: $KTaO_3$ surface after annealing at 443 K, AFM, 100×100 nm², 3.6 V, 0.004 nA............ 23

Fig. 13: $KTaO_3$ surface after annealing at 478 K a) STM, 200×200 nm², 3.35 V, 0.006 nA b) STM, 50×50 nm², 3.25 V, 0.006 nA c) AFM, 20×20 nm², 0.02 V 24

Fig. 14: Results of the DFT calculations carried out by Michele Reticcioli a) model of the annealed surface, the rectangle marks the reconstructed unit cell b) result of DFT calculations of the surface energy for different terrace widths 24

Fig. 15: a) as cleaved surface, STM, 100×100 nm², 3.5 V, 0.1 nA b) surface after annealing at 423 K, STM, 100×100 nm², 3.5 V, 0.1 nA c) linescan of arrow in (a) d) linescan of arrow in (b) 25

Fig. 16: surface after annealing at 523 K a) STM, 70×70 nm², 3.2 V, 0.2 nA b) STM, 40×40 nm², 3.2 V, 0.2 nA c) linescan of arrow in a) 25

Fig. 17: surface after annealing at 623 K a) STM, 100×100 nm², 3.35 V, 0.08 nA b) STM, 50×50 nm², 3.35 V, 0.08 nA c) linescan of arrow in b) 26

Fig. 18: a) surface after annealing at 723 K, STM, 50×50 nm², 3.35 V, 0.07 nA b) surface after annealing at 823 K, STM, 100×100 nm², 3.5 V, 0.1 nA c) surface after annealing at, STM, 823 K, 40×40 nm², 3.5 V, 0.1 nA 26

Fig. 19: $KTaO_3$ surface after 100 L H_2O dosage a) AFM, 200×200 nm², 1.0 V, -1.6 Hz b) AFM, 20×20 nm², 0.001 V c) AFM, 10×10 nm², 0.001 V 27

Fig. 20: $KTaO_3$ surface after 300 L H_2O dosage a) AFM, 80×80 nm², 0.01 V, -0.7 Hz b) AFM, 15×15 nm², 0.01 V 27

Fig. 21: $KTaO_3$ surface after 300 L H_2O dosage a) AFM, 10×10 nm², 0.01 V b) AFM, 4×4 nm², 0.01 V c) AFM, 7.5×7.5 nm², 0.01 V d) model of the (2×1) reconstructed surface with hydroxyl groups, provided by Michele Reticcioli 28

Fig. 22: a) $KTaO_3$ surface after 1 L H_2O dosage at 97 K, STM, 100×100 nm, 3.2 V, 0.005 nA b) $KTaO_3$ surface after 1 L H_2O dosage at 97 K and annealing at room temperature, STM, 100×100 nm², 3.0 V, 0.005 nA c) $KTaO_3$ surface after 1 L H_2O dosage at 97 K, AFM, 16×16 nm², 0.0001 V d) $KTaO_3$ surface after 1 L H_2O dosage at 97 K and annealing at room temperature, AFM, 25×25 nm², 0.0001 V 29

Fig. 23: a) as cleaved surface, STM, 100×100 nm², 3.5 V, 0.1 nA b) surface after 300 L H_2O dosage, STM, 100×100 nm², 3.5 V, 0.1 nA c) surface after 300 L H_2O dosage, STM, 100×100 nm², 3.3 V, 0.07 nA 30

Fig. 24: surface after 300 L H_2O dosage and annealing at 373 K a) STM, 100×100 nm², 2.1 V, 0.1 nA b) STM, 100×100 nm², 3.3 V, 0.07 nA c) STM, 50×50 nm², 3.3 V, 0.07 nA 30

Fig. 25: a) surface after 300 L H_2O dosage and annealing at 473 K, STM, 100×100 nm², 3.3 V, 0.1 nA b) surface after 300 L H_2O dosage and annealing at 473 K, STM, 40×40 nm², 3.3 V, 0.1 nA c) surface after 300 L H_2O dosage and annealing at 523 K, STM, 100×100 nm², 3.3 V, 0.1 nA 31

Fig. 26: DFT calculated phase diagrams for several annealing temperatures provided by Michele Reticcioli 31

Fig. 27: a) surface after annealing at 723 K via electron bombardment, 100×100 nm², 3.5 V, 0.1 nA b) surface after annealing at 423 K via direct heating, 100×100 nm², 3.3 V, 0.1 nA 32

Fig. 28: a) surface after annealing at 673 K via direct heating, 80×80, 3.3 V, 0.1 nA b) surface after annealing at 673 K via direct heating, 100×100, 3.3 V, 0.1 nA c) surface after annealing at 673 via direct heating, 100×100, 3.3 V, 0.1 nA 33

Fig. 29: XPS spectra of an as cleaved surface and after H_2O dosages of 1 L and 300 L 34

Fig. 30: a) XPS spectra the O 1s peak of an as cleaved surface and after H_2O dosages of 1L and 300 L b) peak fit of the 300 L H_2O spectrum in (a) 35

Fig. 31: XPS spectra of an as cleaved surface and after H_2O dosages of 1L and 300 L of the a) K 2p and b) Ta 4f core level peaks 35

Fig. 32: LEIS spectra of an as cleaved $KTaO_3$ surface and an as cleaved surface after an H_2O dosage of 300 L 37

Fig. 33: LEIS spectra of an as cleaved $KTaO_3$ surface and after dosing H_2O onto the ion bombarded surface 38

Fig. 34: LEED patterns of the a) as cleaved surface b) the surface after annealing at 588 K c) after annealing at 588 K and dosing 1 L of water vapor and d) after dosing 300 L H_2O, annealing at 523 K and dosing another 300 L H_2O 39

Fig. 35: LEED patterns of the cleaved surface after annealing at a) 300 K b) 500 K c) 700 K and d) 885 K 39

Fig. 36: LEED pattern of cleaved surface after dosing 300 L of water vapor; the (2×1) structure is clearly visible. 40

11 References

1 Paulauskas, I. E. *et al.* Growth, Characterization, and Electrochemical Properties of Doped n-Type KTaO3 Photoanodes. *Journal of The Electrochemical Society* **156**, B580, doi:10.1149/1.3089281 (2009).

2 Akbarzadeh, A. R., Bellaiche, L., Leung, K., Íñiguez, J. & Vanderbilt, D. Atomistic simulations of the incipient ferroelectric KTaO3. *Physical Review B* **70**, doi:10.1103/PhysRevB.70.054103 (2004).

3 Ang, C., Bhalla, A. S. & Cross, L. E. Dielectric behavior of paraelectric KTaO3, CaTiO3, and (Ln1/2Na1/2) TiO3 under a dc electric field. *Physical Review B* **64**, doi:10.1103/PhysRevB.64.184104 (2001).

4 Grenier, P., Bernier, G., Jandl, S., Salce, B. & Boatner, L. A. Fluorescence and ferroelectric microregions in KTaO3. *Journal of Physics: Condensed Matter* **1**, 2515 (1989).

5 Salce, B., Gravil, J. L. & Boatner, L. A. Disorder and thermal transport in undoped KTaO 3. *Journal of Physics: Condensed Matter* **6**, 4077 (1994).

6 Singh, D. J. Stability and phonons of KTaO3. *Physical Review B* **53**, 176-180 (1996).

7 Uwe, H., Lyons, K. B., Carter, H. L. & Fleury, P. A. Ferroelectric microregions and Raman scattering inKTaO3. *Physical Review B* **33**, 6436-6440, doi:10.1103/PhysRevB.33.6436 (1986).

8 Bareille, C. *et al.* Two-dimensional electron gas with six-fold symmetry at the (111) surface of KTaO3. *Sci Rep* **4**, 3586, doi:10.1038/srep03586 (2014).

9 King, P. D. *et al.* Subband structure of a two-dimensional electron gas formed at the polar surface of the strong spin-orbit perovskite KTaO3. *Phys Rev Lett* **108**, 117602, doi:10.1103/PhysRevLett.108.117602 (2012).

10 Oka, D., Hirose, Y., Nakao, S., Fukumura, T. & Hasegawa, T. Intrinsic high electrical conductivity of stoichiometric SrNbO3 epitaxial thin films. *Phys. Rev. B* **92**, 205102, doi:10.1103/PhysRevB.92.205102 (2015).

11 Prusseit, W., Boatner, L. A. & Rytz, D. Epitaxial YBa2Cu3O7 growth on KTaO3 (001) single crystals. *Applied Physics Letters* **63**, 3376-3378, doi:10.1063/1.110150 (1993).

12 Ueno, K. *et al.* Discovery of superconductivity in KTaO(3) by electrostatic carrier doping. *Nat Nanotechnol* **6**, 408-412, doi:10.1038/nnano.2011.78 (2011).

13 Deacon-Smith, D. E., Scanlon, D. O., Catlow, C. R., Sokol, A. A. & Woodley, S. M. Interlayer cation exchange stabilizes polar perovskite surfaces. *Adv Mater* **26**, 7252-7256, doi:10.1002/adma.201401858 (2014).

14 Fritsch, J. & Schröder, U. Reconstruction of the (001) Surface of Potassium Tantalate. *physica status solidi (b)* **215**, 827-831, doi:10.1002/(SICI)1521-3951(199909)215:1<827::AID-PSSB827>3.0.CO;2-0 (1999).

15 Tasker, P. W. The stability of ionic crystal surfaces. *Journal of Physics C: Solid State Physics* **12**, 4977-4984 (1979).

16 *MTI Corporation*, <http://www.mtixtl.com/ktao3.aspx> (Accessed 2017/09/06).

17 Li, J. A. *et al.* Surface structure and dynamics of KTaO3 (001). *Physical Review B* **68**, 045402, doi:10.1103/PhysRevB.68.045402 (2003).

18 Wemple, S. H. Some Transport Properties of Oxygen-Deficient Single-Crystal Potassium Tantalate (KTaO3). *Physical Review* **137**, A1575-A1582, doi:10.1103/PhysRev.137.A1575 (1965).

19 Höchli, U. T., Weibel, H. E. & Boatner, L. A. Quantum Limit of Ferroelectric Phase Transitions in KTa1−xNbxO3. *Physical Review Letters* **39**, 1158-1161, doi:10.1103/PhysRevLett.39.1158 (1977).

20 Jellison, G. E., Paulauskas, I., Boatner, L. A. & Singh, D. J. Optical functions of KTaO3 as determined by spectroscopic ellipsometry and comparison with band structure calculations. *Physical Review B* **74**, 155130, doi:10.1103/PhysRevB.74.155130 (2006).

21 Dawber, M., Rabe, K. M. & Scott, J. F. Physics of thin-film ferroelectric oxides. *Reviews of Modern Physics* **77**, 1083-1130 (2005).

22 Grabowska, E. Selected perovskite oxides: Characterization, preparation and photocatalytic properties—A review. *Applied Catalysis B: Environmental* **186**, 97-126, doi:10.1016/j.apcatb.2015.12.035 (2016).

23 Grinberg, I. *et al.* Perovskite oxides for visible-light-absorbing ferroelectric and photovoltaic materials. *Nature* **503**, 509-512, doi:10.1038/nature12622 (2013).

24 Bajorowicz, B. *et al.* Perovskite-type KTaO3–reduced graphene oxide hybrid with improved visible light photocatalytic activity. *RSC Adv.* **5**, 91315-91325, doi:10.1039/c5ra18124k (2015).

25 Meevasana, W. *et al.* Creation and control of a two-dimensional electron liquid at the bare SrTiO3 surface. *Nature Materials* **10**, 114-118, doi:10.1038/nmat2943 (2011).

26 Santander-Syro, A. F. *et al.* Two-dimensional electron gas with universal subbands at the surface of SrTiO(3). *Nature* **469**, 189-193, doi:10.1038/nature09720 (2011).

27 Chusuei, C. C. & Goodman, D. W. in *Encyclopedia of Physical Science and Technology* Vol. 17 Ch. X-Ray Photoelectron Spectroscpy, 921-938 (Academic Press, 2002).

28 Jorisch, W. in *Vacuum Technology in the Chemical Industry* Vol. 2015 (ed Wolfgang Jorisch) Ch. 5, 97-128 (WILEY-VCH Verlag GmbH & Co. KGaA).

29 Hoffmann, D. M., Singh, B. & Thomas, J. H. *Handbook of Vacuum Science and Technology*. (Academic Press, 1998).

30 Binnig, G., Rohrer, H., Gerber, C. & Weibel, E. Surface Studies by Scanning Tunneling Microscopy. *Physical Review Letters* **49**, 57-61, doi:10.1103/PhysRevLett.49.57 (1982).

31 Binnig, G. & Rohrer, H. Scanning Tunneling Microscopy. *Surface Science* **126**, 236-244 (1982).

32 Wiesendanger, R. *Scanning Probe Microscopy and Spectroscopy - Methods and Applications*. (Cambridge University Press, 1994).

33 Libioulle, L., Ronda, A., Derycke, I., Vigneron, J. P. & Gilles, J. M. Vertical two-dimensional piezoelectric inertial slider for scanning tunneling microscope. *Review of Scientific Instruments* **64**, 1489-1494, doi:10.1063/1.1144068 (1993).

34 Niedermann, P., Emch, R. & Descouts, P. Simple piezoelectric translation device. *Review of Scientific Instruments* **59**, 368-369, doi:10.1063/1.1140206 (1988).

35 Woodburn, C. N., McKinnon, A. W., Roberts, D. A., Taylor, M. E. & Welland, M. E. A one-dimensional piezoelectric-driven inertial micropositioner with vertical capabilities. *Measurement Science and Technology* **4**, 535 (1993).

36 Binnig, G. & Smith, D. P. E. Single-tube three-dimensional scanner for scanning tunneling microscopy. *Review of Scientific Instruments* **57**, 1688-1689, doi:10.1063/1.1139196 (1986).

37 *ASTM International: Guide to Scanner and Tip Related Artifacts in Scanning Tunneling Microscopy and Atomic Force microscopy*, <www.astm.org> (Accessed 2017/09/10).

38 Howland, R. & Benatar, L. *A practical guide to scanning probe microscopy*. (ThermoMicroscopes, 2000).

39 Rahe, P., Bechstein, R. & Kühnle, A. Vertical and lateral drift corrections of scanning probe microscopy images. *Journal of Vacuum Science & Technology B* **28**, C4E31-C34E38, doi:10.1116/1.3360909 (2010).

40 Giessibl, F. J. Atomic Force Microscopy on Its Way to Adolescence. *AIP Conference Proceedings* **696**, 60-67, doi:10.1063/1.1639678 (2003).

41 Giessibl, F. J. A direct method to calculate tip–sample forces from frequency shifts in frequency-modulation atomic force microscopy. *Applied Physics Letters* **78**, 123-125, doi:10.1063/1.1335546 (2001).

42 Giessibl, F. J. Advances in atomic force microscopy. *Reviews of Modern Physics* **75**, 949-983, doi:https://doi.org/10.1103/RevModPhys.75.949 (2003).

43 Seo, Y. & Jhe, W. Atomic force microscopy and spectroscopy. *Reports on Progress in Physics* **71**, 016101, doi:10.1088/0034-4885/71/1/016101 (2008).

44 Kontomaris, S. V. & Stylianou, A. Atomic force microscopy for university students: applications in biomaterials. *European Journal of Physics* **38**, 033003, doi:10.1088/1361-6404/aa5cd6 (2017).

45 Israelachvili, J. N. *Intermolecular and Surface Forces*. Third Edition edn, (Elsevier Inc., 2011).

46 Gross, L., Mohn, F., Moll, N., Liljeroth, P. & Meyer, G. The chemical structure of a molecule resolved by atomic force microscopy. *Science* **325**, 1110-1114, doi:10.1126/science.1176210 (2009).

47 Giessibl, F. J. High-speed force sensor for force microscopy and profilometry utilizing a quartz tuning fork. *Applied Physics Letters* **73**, 3956-3958, doi:10.1063/1.122948 (1998).

48 Giessibl, F. J., Hembacher, S., Bielefeldt, H. & Mannhart, J. Subatomic Features on the Silicon (111)-(7×7) Surface Observed by Atomic Force Microscopy. *Science* **289**, 422-425 (2000).

49 Albrecht, T. R., Grütter, P., Horne, D. & Rugar, D. Frequency modulation detection using high-Q cantilevers for enhanced force microscope sensitivity. *Journal of Applied Physics* **69**, 668-673, doi:10.1063/1.347347 (1991).

50 Hollander, J. M. & Jolly, W. L. X-ray photoelectron spectroscopy. *Accounts of Chemical Research* **3**, 193-200, doi:10.1021/ar50030a003 (1970).

51 Moulder, J. F., Stickle, W. F., Sobol, P. E. & Bomben, K. D. *Handbook of X-Ray Photelectron Spectroscopy*. (Physical Electronics, Inc., 1995).

52 Yeh, J. J. & Lindau, I. *Atomic subshell photoionization cross sections and asymmetry parameters: $1 \leq Z \leq 103$*. Vol. 32 (1985).

53 *Thermo Fisher Scientific Inc.*, <https://xpssimplified.com/xray_generation.php> (Accessed 2017/10/10).

can impinge on any part of the pump and are captured there [28]. Because the impinging ions sputter the surrounding surface, the titanium layer is constantly refreshed [28]. This provides a clean surface where chemically reactive gases like oxygen or nitrogen can be chemisorbed. Ion getter pumps must only be operated at low pressures, where they provide an effective pumping mechanism. When higher gas pressures are needed inside the vacuum chamber, e.g., for LEIS measurements or water dosages, the ion pump is switched off and pumping is undertaken by the turbomolecular pump.

Titanium sublimation pump

The basic mechanism for a sublimation pump is the chemisorption of residual gas molecules on a chemically reactive metal surface. Due to its high reactivity and the possibility of evaporation directly from the solid state, titanium is the material of choice for most sublimation pumps [29]. When in operation titanium is evaporated and deposited on a substrate where residual gas particles are adsorbed [29]. The evaporation has to be repeated when the Ti layer is fully covered with adsorbates, which happens in different time sequences depending on the pressure [29]. Titanium sublimation pumps are usually used to quickly remove high amounts of residual gases such as oxygen, nitrogen or water vapor [29].

4.2 Scanning tunneling microscopy (STM)

4.2.1 Principle of STM

In principle in an STM measurement a sharp tip is scanned across the surface of interest, whereby both the tip and the sample need to be conductive. When the tip is approached close enough (~1 nm) [30] to the sample surface a tunneling current can be measured. To direct the tunneling current a bias voltage is applied on the sample. The experiments presented in this thesis were performed with positive bias voltage, so the empty states of the sample were measured. While the tip is moved in x- and y-direction over the surface a feedback loop adjusts the height of the tip (in z-direction) to keep the tunneling current constant [30-32]. By recording the tip height as a function of the x- and y-position images of the surface are composed [30-32]. Fig. 4 shows a schematic of an STM instrument.

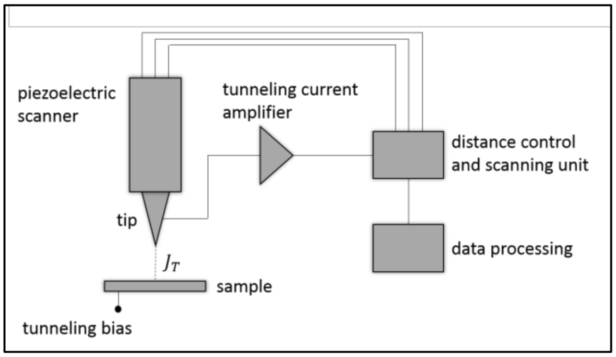

Fig. 4: Schematic of an STM instrument

The tunneling current J_T can be expressed as

$$J_T \propto \exp(-A\varphi^{1/2}z) \qquad \text{Eq. 1}$$

where

54 Allen, J. S. An Improved Electron Multiplier Particle Counter. *Review of Scientific Instruments* **18**, 739-749, doi:10.1063/1.1740838 (1947).

55 Burroughs, E. G. Collection Efficiency of Continuous Dynode Electron Multiple Arrays. *Review of Scientific Instruments* **40**, 35-37, doi:10.1063/1.1683743 (1969).

56 Hoffmann, J. *Messen nichtelektrischer Größen : Grundlagen der Praxis*. (VDI-Verlag, 1996).

57 Brongersma, H., Draxler, M., Deridder, M. & Bauer, P. Surface composition analysis by low-energy ion scattering. *Surface Science Reports* **62**, 63-109, doi:10.1016/j.surfrep.2006.12.002 (2007).

58 Cushman, C. V., Grehl, T. & Linford, M. R. (Vacuum Technology & Coating, 2015).

59 Cushman, C. V. *et al.* Low energy ion scattering (LEIS). A practical introduction to its theory, instrumentation, and applications. *Anal. Methods* **8**, 3419-3439, doi:10.1039/c6ay00765a (2016).

60 Jona, F., Strozier, J. A. & Yang, W. S. Low-energy electron diffraction for surface structure analysis. *Reports on Progress in Physics* **45**, 527-585 (1982).

61 Tanuma, S., Powell, C. J. & Penn, D. R. Calculations of electron inelastic mean free paths. *Surface and Interface Analysis* **37**, 1-14, doi:10.1002/sia.1997 (2005).

62 Henzler, M. LEED studies of surface imperfections. *Applications of Surface Science* **11/12**, 450-469, doi:10.1016/0378-5963(82)90092-7 (1982).

63 Van Hove, M. A., Weinber, W. H. & Chan, C.-M. *Low-Energy Electron Diffraction - Experiment, Theory and Surface Structure Determination*. (Springer-Verlag, 1986).

64 Gross, L. *et al.* Investigating atomic contrast in atomic force microscopy and Kelvin probe force microscopy on ionic systems using functionalized tips. *Physical Review B* **90**, 155455-155451 - 155455-155411, doi:10.1103/PhysRevB.90.155455 (2014).

65 Thomas, J. H. & Hammer, L. H. A Photoelectron Spectroscopy Study of CF4/H2 Reactive Ion Etching Residue on Tantalum Disilicide. *Journal of The Electrochemical Society* **136**, 2004-2210 (1989).